INTEGRATION AND ANALYSIS OF CONFIGURABLE LATTICE GEOMETRY

FOR PROSTHETIC BONE MORPHOLOGY

AN ABSTRACT

SUBMITTED ON THE THIRTEENTH DAY OF MAY 2020

TO THE DEPARTMENT OF BIOMEDICAL ENGINEERING

IN PARTIAL FULFILLMENT OF REQUIREMENTS

OF THE SCHOOL OF SCIENCE AND ENGINEERING

OF TULANE UNIVERSITY

FOR THE DEGREE

OF

MASTER OF SCIENCE IN ENGINEERING

BY

Afsheen Sajjadi
Afsheen Sajjadi

APRROVED:

Ronald Anderson, Ph.D
Director

Michael Dancisak
Michael Dancisak, Ph.D

Katherine K. Raymond
Katherine Raymond, Ph.D

Abstract

Prostheses have enabled many people with bone injuries to achieve a quality of life that would be difficult without the advances in biomedical engineering and materials sciences. Exploration of alternatives to current methods of prosthetic bone development will result in more options from both the physician and patient perspective for the replacement of bone and the use of bone substitutes. Thus, new bone prostheses can be customized to a patient's needs. To address rising healthcare costs, 3D printed bone substitutes are enabling affordable and customizable bone replacements. In this study, we designed a strong yet lightweight structural matrix to substitute bone grafts in cases of comminuted fracture of tibial bone. The artificial matrix is inspired by structural components called voxels that have been demonstrated to be feasible in the areas of aerospace for fixed and morphing wing flight. The basis of this voxel matrix is derived from units of hollow eight-sided faces formed from 12 connected struts. In this study, we have produced and simulated a lattice that can resemble natural bone performance. This bone facsimile has been evaluated using finite element analysis to suggest an optimal voxel density and beam width at which the internal structure has a high elastic modulus to relative density ratio for use as a scaffold during bone reconstruction. A lattice-based implant was designed and evaluated using finite-element analysis for osteosarcoma-afflicted long bones such as the tibia. This study should pave the way for bone implants made of strong but lightweight structures can help patients regain the faculties of natural bone. Ultimately, this structure would be constructed from biocompatible materials that provide nutrients for natural bone regeneration processes. With this, the structure would reabsorb completely into the healing bone, after providing a matrix upon which osteoblasts can form new bone.

INTEGRATION AND ANALYSIS OF CONFIGURABLE LATTICE GEOMETRY

FOR PROSTHETIC BONE MORPHOLOGY

A THESIS

SUBMITTED ON THE THIRTEENTH DAY OF MAY 2020

TO THE DEPARTMENT OF BIOMEDICAL ENGINEERING

IN PARTIAL FULFILLMENT OF REQUIREMENTS

OF THE SCHOOL OF SCIENCE AND ENGINEERING

OF TULANE UNIVERSITY

FOR THE DEGREE

OF

MASTER OF SCIENCE IN ENGINEERING

BY

Afsheen Sajjadi

Afsheen Sajjadi

APRROVED:

Ronald Anderson, Ph.D
Director

Michael Dancisak

Michael Dancisak, Ph.D

Katherine K. Raymond

Katherine Raymond, Ph.D

Acknowledgments

This work would not have existed if not for the previous work done by the Coded Structures Laboratory at NASA Ames Research Center and the MIT Media Lab. Specifically, I am grateful to Dr. Kenny Cheung who gave me the opportunities through internships to contribute to the rising field of digital materials. I owe my exploration into the material sciences to Dr. Christine Gregg, who patiently taught me all about mechanical behaviors. I am grateful to Joseph Kim for introducing me to the simulation side of materials and helping me come up with the initial research proposals. I am especially thankful to Joseph for all the advice and coding lessons I needed to complete this project.

I owe the successful completion of this thesis to my advisor Dr. Ronald Anderson, who guided me in pursuing the practical application of this geometry to surgical therapies for osteosarcomas. His advice on proper simulation techniques was a critical aspect for this thesis. I am appreciative of Dr. Michael Dancisak, Director of the Tulane University Center for Anatomical and Movement Sciences (CAMS), for his early guidance in approaching this broad research topic. Dr. Dancisak's patience, advice, insight, and support were essential to my initial progress on this thesis. I am thankful to my third committee member Dr. Katherine Raymond for her support and advice throughout the years. I also appreciate Christian Logarbo and Sam Belden for their help in the dissection of the cadaveric bone specimens. I am grateful for the resources of the Tulane MakerSpace and the insight of its affiliates. I'd like to additionally thank the Tulane Department of Biomedical Engineering for their 4 years of comprehensive education in preparing me for this project.

Finally, I'd like to thank my mom, my dad, my sister Auzita, and all my friends. Without their continued support, I could not have completed this thesis.

Table of Contents

List of Tables

List of Figures

Chapter 1: Introduction

Prostheses have enabled many people with bone injuries to achieve a quality of life that would be difficult without the advances in biomedical engineering and materials sciences. Exploration of alternatives to current methods of prosthetic bone development will result in more options from both the physician and patient perspective for the replacement of bone and the use of bone surrogates; leading to new bone prosthetics that can be customized to a patient's needs. Advancements in bionics and new artificial bone treatments are allowing patients to have more control over what types of prosthetic limbs they use and how patients can modify their use without having to return to the clinic ("3D-Printable Prosthetics | e-NABLE", 2019). To address rising healthcare costs, 3D printed bone substitutes are enabling affordable and customizable replacements for fractured bone ("3D-Printable Prosthetics | e-NABLE", 2019). However, design optimization and analysis of artificial bone scaffolds, based on a strong structural geometry, implanted as substitutes to fractured bones have not yet been done.

In the United States, trends collected by the Mayo Clinic show that there are over 300,000 cases annually of tibial or fibular fractures (Amin et al., 2014). In cases of comminuted fracture of a long bone, surgeons often implant metallic substitutes to regain rigidity and stability in the limb. While these metallic substitutes can be customized to a certain extent for various applications, they may not be the most efficient implant considering high rates of postoperative pain suffered by patients (Majuta et al., 2015). Most prosthetic technology does not intend to mimic natural, internal bone structure which has undergone continuous evolutionary selection. Specifically, a study focusing on the design

of an artificial replacement, for the diaphysis of long bones, that can interface with the secondary ossification centers in fully developed adults would be of value to optimize the performance of prosthetics and bone implants. Trabecular bone, especially in the long bones, are composed of small strut-like tissue elements that form a complex meshwork that is organized to optimally resist loads imposed by physical activities. Many studies exist that use finite element analysis to simulate load and responses on trabecular bone, however, emulating the trabecular meshwork in an easy to reproduce artificial application for bone implants or prototype prosthetics has not yet been done.

This study explores whether prostheses can be improved by generating a strong, yet lightweight lattice substructure for artificial bone. Octahedron shaped unit cells called voxels (see operational definition) packed into a lattice structure already have been shown to provide a high ultimate compressive strength with a low relative density compared to a homogenous sample of the same material (Cheung 2013). These unit cells serve as the basis for digital materials that could be used to construct highly customizable structures at different scales while maintaining the favorable properties of a high strength to low-density ratio. Several case studies for this technology already have been determined and shown to be feasible in the areas of aerospace (Jenett, 2016).

In this study, a computer-generated bone facsimile has been generated with an octahedron lattice internal structure based on a 3D scan of a cadaveric tibia. This bone facsimile has been tested using finite element analysis to determine a density at which the internal structure has favorable properties of ultimate compressive strength for use as a scaffold during bone reconstruction. For this study, a cadaveric tibia was dissected and cleaned to acquire an accurate 3D model to use as a frame for the generation of an

octahedron lattice structure. The resulting custom structure was compressed to obtain a structural elastic modulus using a finite element analysis, for comparison against natural bone. The lattice densities were modified and tested to determine the optimal model with the lowest density that gives the equivalent strength of traditional bone. A cylindrical lattice specimen composed of the octahedron lattice internal structure was 3D printed and mechanically compressed to verify the accuracy of the simulations. A lattice comparable to the 3D printed specimen was digitally generated and simulated with the same parameters as the physical experiments.

Surgical intervention of osteosarcomas often necessitates decimation of the bone surrounding the tumor and requires metal implants that reduce the functionality of the patient's lower limb. This study simulates the feasibility of an octahedron lattice implant as an alternative in surgical intervention of osteosarcomas. An imitation of a tibia afflicted with osteosarcoma was generated through targeted editing of the 3D scan of the cadaveric tibia. A methodology was designed to emulate surgical removal of the tumor from the bone. The natural geometry of the removed portions of the bone was estimated for generation of the structural bounds of the lattice implant. The natural geometry was determined using a surface constructed from the shortest straight-line distances between the superior and inferior edges of the removed region. An octahedron lattice structure was manually designed to be used as a template for the implant. This template was digitally edited to conform to the implant's structural bounds. The structural bounds were further used to form a thin outer shell for the lattice implant. The bone geometry remaining after surgical intervention was computationally simulated under body-weight loading conditions to establish regions from which the lattice implant is intended to alleviate high stresses. The

lattice implant was compressed via finite element analysis to determine the distribution of stress concentrations throughout the lattice. By comparing the stress distribution to the yield strength of the underlying material, this study ascertains the structural viability of the lattice implant under typical body-weight loading conditions.

This study begins to pave the way for the next generation of bone implants or scaffolds, where strong but lightweight artificial structures can help patients regain comparable functions that natural bone provides due to its strength and density. The bone facsimile in this study has been simulated and constructed with the material properties of polylactic acid, a biocompatible plastic that previously has been used in bone scaffolds (Gregor et al., 2017). Additionally, the bone facsimile in this study has been simulated with the material properties of an injected molded thermoplastic tested for aerospace applications and that of a titanium alloy commonly used in orthopedic implants. By producing and simulating a lattice that can resemble natural bone performance, the foundation for future applications can be constructed.

Operational Definitions

Voxel – A hollow eight-sided frame formed from 12 connected struts.

Lattice - Multiple units of voxels which have been interfaced with one another to form complex hollow structures.

Node – The vertices of the voxel or point at which the struts of a voxel converge. A single voxel contains 8 nodes.

Voxel Pitch - The size of a voxel-based on the distance between opposite nodes

Beam Width – The thickness of each strut composing a voxel

Voxel density –In this study, we consider the number of voxels to be a sufficient representation of relative density. Relative density is a comparison showing the amount of free space within the bounding box of a lattice relative to a solid fill of the same material.

Chapter 2: Review of Literature

2.1 – Inspiration

Evolution has made sure that the structure of natural bone can be considered one of the most complex and high performing materials. Cancellous bones, specifically the trabeculae within, are of interest because they are strong and lightweight. Trabeculae are composed of strut or rod-like units that result in a series of trabeculae, which creates hollow space within cancellous bone to allow vessels to reach the hematopoietic tissue within the spongy bone (Meyers and Chen, 2014).

The study of digital cellular solids takes inspiration from this natural bone phenomenon, to generate an artificial structure that could be used for various engineering applications (Cheung, 2012). The primary goals of this artificial structure are to have the same base properties of high relative strength for a low relative density. The idea behind digital cellular solids is to develop a set of discrete base units like trabeculae, that can be assembled into a strong lattice structure (Cheung and Gershenfeld, 2013). Scientists have begun to solve the challenge of creating strong yet lightweight materials through a collaboration of the Massachusetts Institute of Technology and the NASA Ames Research Center. The base units that have been developed are referred to as voxels or volumetric pixels. A voxel is a hollow eight-sided frame formed from 12 connecting struts, that can easily interface with other voxels to form complex hollow structures. When assembled, voxels form a rigid lattice structure, where the strength and rigidity improve as more voxels are added to the lattice (Jenett, Cellucci, et al., 2016). The performance of this artificial structure compared to traditional materials can be seen in *Figure 2.1.1*. Voxels can be made

from different materials and assembled heterogeneously to match desired proper material properties such as increased flexibility in one region. Voxels also can be scaled by increasing the component strut lengths or by increasing the strut thickness (Gregg, Kim, and Cheung, 2018). Voxel lattice structures have already been applied and tested as part of high stress structures on fixed-wing aircraft and morphing wing aircraft (Cheung et al., 2017). There is unlimited potential for applying this lattice structure for applications outside of aerospace due to the broad utility of its high strength to low-density material properties.

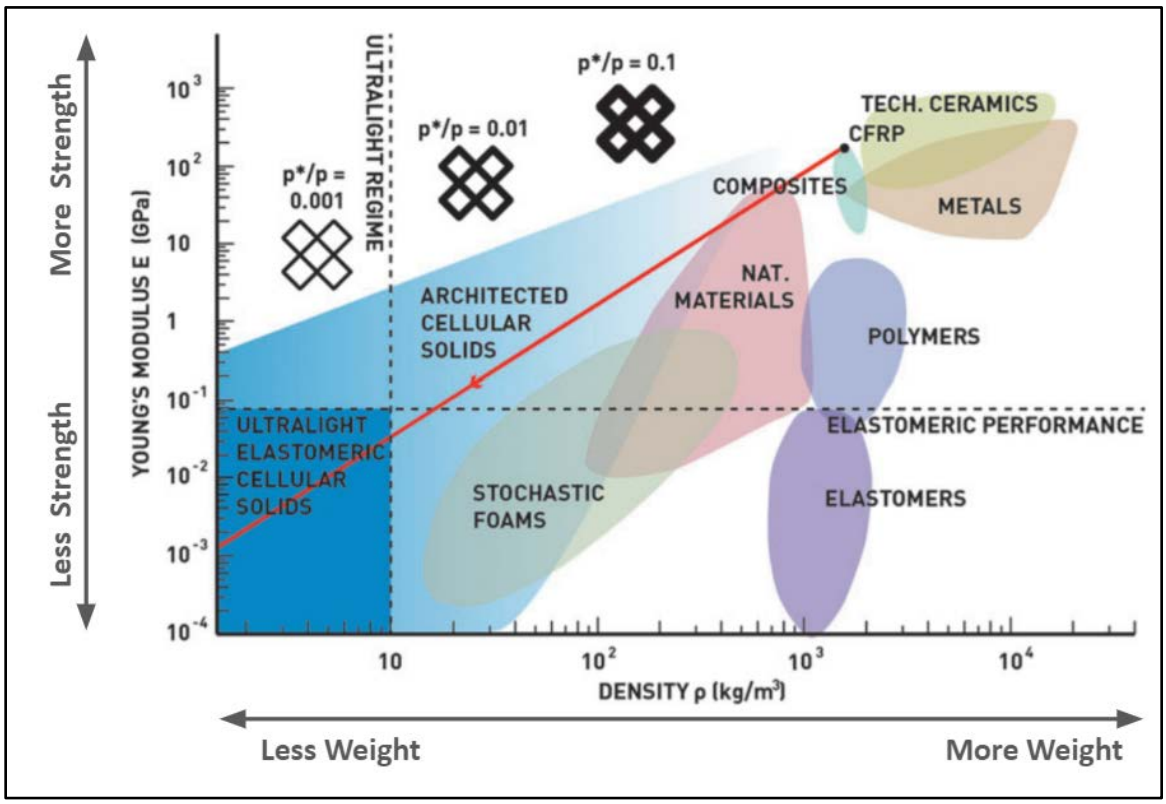

Figure 2.1.1 – Ashby chart showing strength to weight performance for engineering materials vs cellular solids. (Jenett, Calisch, et al., 2016)

The concept of generating an artificial structure for regenerative tissue treatments is not new. Use of artificial scaffolds has been a cornerstone of biomedical research in tissue engineering for decades. Recently, artificial scaffolds for bones have been shown to

improve the regeneration process in large segmental bone defects compared to autologous bone grafts (Pobloth et al., 2018). Specifically, this study revealed that designing a scaffold to optimize stresses and strains on bone fracture regions aids in bone healing. Cellular solids inspired the honeycomb-like scaffold structure; by changing the strut diameter researchers were able to target various levels of stiffness to test its effect on bone regeneration. Researchers tested targeted scaffold configurations *in vivo* in sheep for a large bone defect, resulting in early bridging of the defect, formation of endochondral bone, and regeneration of bone at the defect (Pobloth et al., 2018). Other studies have considered using artificial scaffolds that have the dual effect of providing nutrients to the healing bone. 3D-printed scaffolds consisting of a hollow strut structure have been implanted in a rabbit radius and used to release bioactive ions from the hollow struts to enhance the growth factor delivery and vascular development through osteogenesis and angiogenesis (W. Zhang et al., 2017). These studies have demonstrated the regenerative benefits and feasibility of implanting lattice scaffolds for the purposes of segmental bone regeneration.

2.2 – Bone Mechanics

As the primary structural components of the human body, bones have functionally developed to resist fracture. The material of bone is a ceramic-polymer composite of collagen, hydroxyapatite, and water. In different animals, bones have evolved to allow for different functionalities. For example, bird bones are lightweight and flexible for flying (Meyers and Chen, 2014). The low relative density of the internal structure of bird bones, combined with its flexible properties, provide birds a similar functionality that is ideal in human-manufactured flight. As a consequence, bird bones helped inspire the application of cellular solids to aeronautical applications (Cheung, 2012). The internal structure of

human bones is consequently ideal for loading associated with human movement. It follows that it is ideal to emulate these natural structures in artificial aids for human movement and loading applications. Advances in material manufacturing provide allow for complicated structures to be artificially generated and printed in high stiffness materials (Pobloth et al., 2018).

Bone, unlike manmade materials, constantly remodels itself every 7-10 years over the course of one's life (Kenkre and Bassett, 2018). Initially, during growth, a tissue called the primary osteon forms on an existing bone. The secondary osteon forms by absorbing the existing bone and replacing it with new bone as a natural response to external loads (Meyers and Chen, 2014). Bone-degrading cells called osteoclasts create a cavity in existing bone tissue through resorption. On the internal surface of this cavity, bone-forming cells called osteoblasts deposit concentric lamellae to form a Haversian canal which contains vasculature to support the bone. Bone remodeling is dependent on body region and can last from two to four months for human bone (Meyers and Chen, 2014).

Due to the complicated nature of bone as a material, its material properties are particularly variable. It is said that the elastic modulus of human cortical bone varies from 7 to 24 GPa, whereas hydroxyapatite on its own has a modulus of 130 GPa. Collagen, a non-linear elastic material, has a tangent modulus of 1 to 1.5 GPa. Elaborate models exist to determine these properties given specific mineral ratios. The tensile strength of human bone varies from 20 MPa to 270 MPa. Individually, collagen has a maximum tensile strength of 50 MPa. Experiments show that cortical bone is stronger in the longitudinal direction than the transverse direction and that it is stronger in compression compared to tension. The variability of bone strength is highly dependent on a myriad of factors ranging

from loading stresses and the rate of loading to the condition of bone (Meyers and Chen, 2014).

As opposed to compact bone, which makes up the outer shell of most bones, cancellous bone is the porous region enclosed within. The combination of these two regions reduces unnecessary weight while maintaining the structural properties needed to handle the various loads we must bear. Cancellous bone is a foamlike cellular solid consisting of a network of rods and plates which are interconnected. Bones are classified as cancellous if they have a relative density of less than 0.7 (Gibson and Ashby, 1997). The network of rods is a low density, open cell region while the plates are a higher density, closed cell structure. Studies of trabeculae found in loaded bone strongly suggest development along the principal stress trajectories (Gibson and Ashby, 1997). The development of plates seems to occur in areas of high stress whereas rods tend to form in low-stress regions. Both cancellous bone and compact bone are composed of similar materials. Gibson describes that cancellous bone anisotropy is determined from the structure, so the longitudinal direction of trabeculae is stiffer and stronger in that alignment (Gibson and Ashby, 1997). Gibson and Ashby conclude that Young's modulus for trabecular bone is 12 GPa while the compressive strength is said to be 136 MPa with a tensile strength of 105 MPa as per *Table 2.2.1.*

r

Table 11.3 Solid cell-wall properties for trabecular bone

Property	Value
Young's modulus	12 GPa
Compressive strength	136 MPa
Tensile strength	105 MPa

Table 2.2.1 – Properties of Cancellous Bone (Gibson and Ashby, 1997)

The experimental results of many cancellous bone studies are shown in *Table 2.2.2* that shows the modulus of individual trabeculae in the human femur is 13 GPa.

Table 11.2 Young's modulus of trabeculae

Reference	Type of bone†	Method	E_s (GPa)
Mechanical tests			
Ryan and Williams (1989)	B F	tension unmachined	0.76 (0.39)
Kuhn *et al.* (1987)	H T	3-point bend machined	3.17 (1.5)
	H cortical		3.8
Choi *et al.* (1990)	H PT	3-point bend machined	4.59 (1.60)
	H cortical		5.44 (1.25)
Townsend *et al.* (1975)	H PT	buckling unmachined	11.4 (wet)
			14.1 (dry)
Runkle and Pugh (1975)	H DF	buckling	8.69 (3.17) dry
Ultrasound tests			
Ashman and Rho (1988)	B F	ultrasound on	10.9 (1.6)
	H F	trabecular bone	13.0 (1.5)
Finite element analysis			
Pugh *et al.* (1973b)	H DF	2D FEM	$E_s < E_{compact}$
Williams and Lewis (1982)	H PT	2D FEM	1.30
Mente and Lewis (1987)	H F	2D FEM	5.3 (2.6) dry
Rietbergen *et al.* (1995)	H PT	3D FEM	2.23–10.1

†All specimens are of individual trabeculae unless stated otherwise. B = bovine; H = human; F = femur; T = tibia; P = proximal; D = distal.

Table 2.2.2 – Modulus of Cancellous Bone under various experiments (Gibson and Ashby, 1997)

The material properties of wet compact bone are shown in *Table 2.2.3*. The modulus of human wet compact bone is reported to be 17 GPa in the longitudinal direction, and 11.5 GPa in the radial and tangential direction. The compressive strength of human wet compact bone is 193 MPa (Gibson and Ashby, 1997). However, the strength and toughness of wet bone value may decrease by loss of fluid due to the interactions between the fluid and the structure (Nyman et al., 2006).

Table 11.1 The properties of wet compact bone†

	Human	Bovine
Density, ρ_s (kg/m^3)	1800–2000	2060
Young's modulus, E_s (GN/m^2)		
longitudinal	17.0	22.6
radial	11.5	10.2
tangential	11.5	10.2
Shear modulus, G_s (GN/m^2)		
longitudinal–radial	3.3	3.6
longitudinal–tangential	3.3	3.6
radial–tangential		
Poisson's ratio, ν_s		
ν_{sLR}	—	0.36
ν_{sLT}	0.41	0.36
ν_{sTR}	0.41	0.51
Compressive strength, σ_{ys} (MN/m^2)		
along	193	254
normal	133	146
Tensile yield strength, σ_{ys}^T (MN/m^2)		
along	148	144
normal	49	46
Toughness, G_{cs} (J/m^2)		
along	—	1690
normal	—	4330
Fracture toughness, K_{1Cs} (MN/m$^{3/2}$)		
along	—	3.5
normal	—	6.1

†Data for all mechanical properties are from static tests on wet compact bone. A more complete summary of the properties of compact bone is available in Currey (1984), from which this table was compiled.

Table 2.2.3 – Compact Bone Properties (Gibson and Ashby, 1997)

The tissue elastic modulus of trabeculae bone present in the human tibia is reported to be 14.8 ± 1.4 GPa (Oftadeh et al., 2015).

Gibson and Ashby conclude that bone tends to form equal cells when loads on cancellous bone are equal in all three principal directions. However, when these loads are uneven, the cells thicken and align to ensure optimal support, with relative density reflecting load magnitude. In osteoporotic patients, bone mass and subsequently bone strength decrease over time, increasing the risk of fracture. It is widely accepted that as one ages, trabecular bone density decreases. In addition, one study shows that bone volume

decreases with age, but trabecular connectedness also decreases. In an earlier study, Hahn et al developed a parameter called the Trabecular Bone Pattern factor which describes the relation of convex to concave surfaces between the rods and the plates of the trabeculae. Hahn considers a well-connected spongy lattice to have many concave surfaces whereas a badly connected trabecular lattice consists of many convex surfaces in relation to two-dimensional bone sections (Hahn et al., 1992). This parameter could be useful in quantifying the connectedness of any artificial lattice compared to natural bone.

Several studies have performed biomechanical testing of various human bones including the femur bone. The results of such tests are critical in the comparison of any artificial lattice structure to natural bone in determining its feasibility as an alternative or supplementary material. The biomechanical testing in these studies consists of impact testing and bend testing, with and without bone implants. According to a study by Arun et al, the hardness of different femoral region varies with the hardness of the femoral shaft generally increasing towards the distal region of the bone. Thus, Arun suggests that the femur's maximum hardness is present at the distal region whereas the minimum hardness is located at the proximal region of the femur. This study suggests that bone implants can result in improper loading of the bone leading to crack formation and improper healing (Arun and Jadhav, 2016). Any artificial bone treatment should consider the necessity of the bone to have stresses in certain locations. *Table 2.2.3* shows the properties of the femur bone under bending in Arun's study.

BENDING TEST				
Specimen Type	**Deflection in mm**	**Maximum bending stress in N/mm^2**	**Young's modulus in Gpa**	**Fracture Toughness in Mpa-mm$^{1/2}$**
Without Implant	2.52	113.23	129.54	141.91
With Implant	0.83	72.05	250.28	90.30
With Crack	1.72	22.30	37.38	31.86

Table 2.2.3 – The material properties associated with a three-point bend test performed on a femur (Arun and Jadhav, 2016)

Another study published in the *Journal of Biomechanics* tests the shear strength of human trabecular bone. In addition, this study analyzes the failure of bones when subjected to sudden loading and when an implant is being used. The results of the study suggest that trabecular bone is stronger in compression than in shear (Sanyal et al., 2012). Further, the trabecular microarchitecture of a bone was the primary factor determining the ratio of shear to compressive strength rather than bone volume fraction. The researchers compressed their trabecular test specimens along the main trabecular orientation representing the primary loading direction. It is of interest to note that the primary failure mode in shear was the obliquely oriented trabeculae, while the primary failure mode in compression resulted from the yield of horizontal trabeculae and low bone volume fraction specimens. Another contributing determinant was the yield of vertical trabeculae and high bone volume fraction specimens (Sanyal et al., 2012). This is useful in assigning the orientation of any artificial lattice that might be implanted in bone.

In one study regarding bone remodeling, researchers used a stochastic lattice model to simulate the adaptations of living bone to mechanical stimuli over time (Weinkamer et al., 2004). These researchers discovered that a network-like structure emerged, with the bone volume eventually reaching steady-state. It can be concluded that bone modeling favors a lattice geometry to handle necessary loading. However, the researchers neglect any bending moment and shear forces present in the trabeculae in their model.

2.4 – 3D Printing for Bone Treatment Applications

The foray of rapid prototyping technologies into the medical research field has allowed for more personalized solutions for patients as well as encouraging rapid manufacture of customized test models. Doctors have been able to perform bone and joint

reconstruction by using 3D printed pieces in a surgical procedure. Although standard mass-produced prosthetics continue to be the more affordable solution for patients, the customization in prosthetics through rapid prototyping is quickly decreasing consumer costs. Researchers have had success in developing custom implants using medical imaging for bone reconstruction (Lantada and Morgado, 2012). Due to density differences between bone tissue and surrounding tissue, software has been developed to extract the detailed geometry of bone for the purposes of replication or analysis. With this detail geometry, specialized implants can easily be designed ("3D-Printable Prosthetics | e-NABLE", 2019).

One of the most common materials used in 3D printing is Polylactic Acid (PLA). The material is also biocompatible with human bone, as shown by prior experiments that used it as a bone scaffold. As such, it is an excellent candidate for initial simulations of the proposed voxel lattice as a bone scaffold. The MakerBot corporation performed compressive strength testing of printed PLA based on ASTM standards D695 as a comparison to the thermoplastic polymer Acrylonitrile butadiene styrene (ABS). The results of the Makerbot study show a compressive ultimate strength of 93.77 MPa and ultimate tensile strength of 65.71 MPa ("PLA and ABS Strength Data", 2014). A study by researchers at MIT puts the yield strength of injection mold grade PLA at 70 MPa and the elastic modulus at 3.5 GPa while noting high variability due to PLA manufacture methods (Farah, Anderson, and Langer, 2016). The material property aggregator service MatWeb describes the typical value tensile yield strength as 37.5 MPa, the typical ultimate tensile strength as 46.8 MPa, and the typical modulus of elasticity as 2.79 MPa ("Overview of Materials for Polylactic Acid (PLA) Biopolymer", 2019).

Recent clinical studies have demonstrated 3D printed titanium bone implants as a functional alternative to traditionally manufactured implants (Popov et al., 2018). Additionally, complex geometries 3D printed in titanium for trabecular bone reconstruction has been shown in the human femoral head as a potential treatment for osteonecrosis (Y. Zhang et al., 2018). This study used the titanium alloy, Ti-6Al-4V, which is commonly used for orthopedic implants. The material property aggregator service MatWeb describes the titanium alloy, Ti-6Al-4V, as having an elastic modulus of 113.8 GPa and a Poisson's ratio of 0.342. The Poisson's ratio of the titanium alloy represents the ratio of transverse strain to axial strain experienced by the alloy such that it undergoes lateral expansion equivalent to nearly a third of the axial deformation when under compression.

2.5 – Finite Element Analysis of Bone

It becomes useful to run multiple trials of a test for a specimen without having to acquire many samples that likely vary in their consistency, composition, and size. Finite Element Analysis simulating biomechanical testing of high-detail bone geometry obtained from medical images allows for this repeatability and environmental control. Several studies have analyzed the performance of trabecular bone in varying conditions as well as the performance of artificial bone implants (Samiezadeh et al., 2014). One study describes a finite element analysis method that determined the biomechanical properties of an intramedullary nail found in femoral shaft fractures (Samiezadeh et al., 2014). In this method, the researchers compared a nail made from a carbon fiber/flax/epoxy composite against a titanium nail. Their results suggest that a nail made using target material properties can aid in bone healing for large fractures because the nail increases the average

normal force at fracture sites. Another finite element study simulated the post-yield behavior of trabecular bone, demonstrating that changing the element size had a minimal effect, whereas changing the material model had a large impact (Verhulp et al., 2008).

2.6 – Cancers of Bone

Osteosarcoma is a mesenchymal bone tumor that can occur in the epiphyseal growth plate of the femur or tibia. Osteosarcoma has been found to have a high lung metastasis rate during the first two decades of life (de Azevedo et al., 2020). It has been found that respiratory involvement is responsible for the greatest amount of osteosarcoma-related deaths, with 80% of cases occurring in the lungs (Lindsey et al., 2016). Subsequently, the survival rate over a five-year period for patients with lung metastases is 20%, in comparison to 65% in patients with only localized bony disease (DeBoer et al., 2011). This disease has quickly become the most common malignant primary bone tumor in adolescents, with approximately two out of a million individuals diagnosed annually (Klen et al., 2006). Epidemiology studies have shown that osteosarcoma is the eighth most prevalent childhood cancer (Ottaviani et al., 2010). The majority of osteosarcoma cases have been found in the femur, 75% of cases located distally, as well as the tibia with 80% located proximally, which is the same location as primary bone growth and development (Ottaviani et al., 2010).

Osteosarcomas typically develop between the ages of 10 to 20 years old and often present as non-metastatic at the time of diagnosis (Wittig et al., 2002). Clinical symptoms in patients diagnosed with osteosarcoma vary with each individual but commonly begins with weeks to months of chronic pain, causing difficulties even while sleeping or at rest (Klein et al., 2006). Other symptoms include a decreased range of motion and muscle

atrophy causing loss of function of an affected limb (Klein et al., 2006). Clinical signs most commonly present as a firm and tender mass at the affected area, as well as erythema, local tenderness, limping, and frequent bone fractures (Wittig et al., 2002).

In order to diagnose and classify osteosarcomas, several clinical tests can be performed, including bone scintigraphy, magnetic resonance imaging (MRI), computed tomography (CT) scans, and positron emission tomography (PET) scans. When imaging results show potential malignancy, a biopsy is typically performed in order to examine samples of bone cells in a pathology laboratory (Wittig et al., 2002). In more severe cases, a chest x-ray may also be ordered, due to the common systemic location of metastasis to the lungs (Wittig et al., 2002). Collectively, these tests can provide a cancer stage and classification in order to better understand treatment options for the osteosarcoma (Klein et al., 2006).

Traditional treatment methods begin with chemotherapy medications in a preoperative stage, which induces tumor necrosis prior to surgical intervention, and a postoperative stage following surgery. Resection of the tumor aims to achieve a disease-free outcome, with a secondary goal of preserving limb function (Wittig et al., 2002). In 2018, Huang et al. examined a group of patients undergoing this multidisciplinary treatment approach of the disease specifically affecting the proximal tibia. The study concluded that the results were overall positive, with improved or recovered limb function postoperatively in 54 out of 69 total cases (Huang et al., 2018).

Alternatively, Ene et al. (2015) studied seven cases of osteosarcoma in the proximal tibia undergoing a similar multidisciplinary treatment in which most patients demonstrated a decrease in physical activity postoperatively. However, these cases also reported minimal

effects on overall limb functionality, and only lifestyle changes were required. It was concluded by the study that while the function of the affected limb does not equal the normal limb comparatively, the quality of life does not change after treatment (Ene et al, 2015).

Huang et al. (2018) detail the surgical process to remove the tumor and insert the rotary hinges used for their patients after several rounds of preoperative chemotherapy. The procedure begins by creating an incision in the distal third of the femur and extending to the proximal tibia. The patellar ligament was detached proximally, the knee capsule was incised adjacent to its tibial insertion, and the biopsy was performed. After resection of the tumor, the artificial joint was implanted and attached to the patellar tendon. Muscle tissue was used to cover the prosthesis and if inadequate, a rotation flap was used to stabilize the area prior to grafting the skin and concluding the procedure (Huang et al., 2018).

Ene et al. (2015) also discuss the surgical protocol in their limb-sparing procedures, which consisted of a resection of the proximal tibial tumor and reconstruction of the knee joint and upper tibia. A titanium knee hinge prosthesis was used along with a muscle rotation flap to protect the prosthesis and attached patellar tendon. Wittig et al. (2002) similarly endorse the use of metallic endoprostheses for tibial reconstruction due to the minimal risk for complication, immediate stable fixation, sturdiness to bear weight, and quick recovery to regain use of the limb.

One potential mechanism of the development of osteosarcoma includes alterations in the differentiation pathway of mesenchymal stem cells to become mature osteoblasts (Yang et al., 2017). Due to a greater bone turnover rate during the bone growth phase, the potential for defects to develop throughout the signaling pathway increases significantly

(Ottaviani et al., 2010). Mesenchymal stem cells in the stroma of bone marrow are undifferentiated, allowing for potential differentiation into bone, muscle, and fat cells. As the factors involved in osteogenesis begin to contribute to the formation of osteoblasts, deregulation and exposure to pro-inflammatory cytokines can lead to proliferation of the malignant cancer cells (de Azevedo et al., 2020).

Chapter 3: Materials & Methods

3.1 – Specimen Acquisition

To begin, a cadaveric specimen with no known skeletal conditions was obtained from the Tulane University Center for Anatomical and Movement Sciences, and the right leg was dissected and disarticulated at the femoral head. The femur, tibia, calcaneus, and fibula were acquired. Adipose, muscular, and cartilaginous tissue was removed completely through an enzyme bath maceration process disarticulating all joints. The maceration solution consisted of 1-part enzymatic detergent and 20-parts water then heated to 180°F for 8 hours. The bones were removed from the enzyme bath and allowed to dry before being placed in an acetone bath in a steel tray modified to minimize the rate of acetone evaporation. Over the course of 24 hours under a fume hood, the acetone completely evaporated, leaving behind a layer of oil. This process was repeated to remove any excess fat from the bones. From the defatting, the distinctive features of the bone became visible.

3.2 – 3D Scanning the Specimen

A handheld 3D scanner (Creaform Go!SCAN 3D, Québec) was used to acquire a three-dimensional digital surface point cloud of the tibia at a resolution of 500 microns. The scanner uses spectrally-broadband white light illumination on an object to measure the surface height of points on the object to construct a digital point cloud. A rotating wooden platform was painted matte black and fitted with 5mm reflective markers to be used as a stage for each bone to be scanned. Each side of the bone was scanned independently. Reflective markers were placed on the target bone to allow the scanner to maintain the position of the scan data in 3D space.

Figure 3.2.1: Healthy tibia from a cadaveric specimen on the scanning platform with reflective markers

Creaform's VXModel software was used to clear any imaging artifacts and consolidate scan data. Distinctive features and reference markers that were present on both sides of the bone were used to align the two sets of scan data in VXModel, to create a single digital surface mesh for the whole bone. A digital surface mesh is a set of faces, edges, and vertices that defines a three-dimensional object digitally. This resulting mesh was made watertight using VXModel's hole autofill feature, to compensate for any missing scan data due to reflective markers covering the bone surface. The resulting watertight model was exported as a standard binary STL mesh file. Then, using Rhino 3D, a mesh editing software, a section of the tibia was cut such that the shaft could be simulated between the nutrient foramina for the distal and proximal epiphyseal arteries. Using a cadaveric specimen rather than a plastic facsimile helped inform the decision regarding where to cut the bone in the mesh editing software. Based on the cadaveric specimen, the digitized model is 368 mm (the length between the nutrient foramen) and the cross-section at mid shaft has a diameter of 32 mm.

3.3 – Generation and Analysis of the Custom Lattice

To create a file ready for simulation based on our scanned specimen, the STL mesh file was imported into a custom program written in Java adapted from code from NASA's Coded Structures Laboratory (Gregg, Kim, and Cheung, 2018). Specifically, the program converts the STL mesh file, representing the scanned bone, into a point cloud representing voxel locations, generates a voxel lattice with these locations, adds displacement and fixed boundary constraints to the proximal and distal ends of the structure respectively, and sets the material properties of the voxels. The result is an ABAQUS input file that can be imported for simulation.

The program uses two primary parameters that adjust the density of the voxel lattice within the resulting ABAQUS input file. The pitch parameter represents the size of the voxel based on the distance between opposite vertices. The beam width parameter represents the thickness of each strut that composes a voxel. The code from the Coded Structures laboratory was used to generate an ABAQUS compatible lattice from the STL mesh file based on these parameters.

Because, by definition, the STL mesh file is composed of connected triangles called facets, the program extracts the facet information from the STL mesh file to store into a series of arrays as points while also storing the normal direction of each facet. Based on these outer boundary points, the program logically determines locations for the later generation of voxels by calculating the center points of the voxels that will fill the lattice. Based on these center points, the program then creates a voxel with the pre-designated parameters at each point to form a lattice within the boundaries of scanned bone. To generate a voxel at a given center point, the vertices of the unit cells are first placed relative

to the center point based on a pitch parameter designating the size of the voxel. Then, the vertices are connected using beams. The beams are given thicknesses based on a beam width parameter. Because this process only produces unlinked individual voxels, the program runs through redundant vertices which have the same coordinates in space and links them. A representative model of the lattice that results is shown in *Figure 3.3.1*.

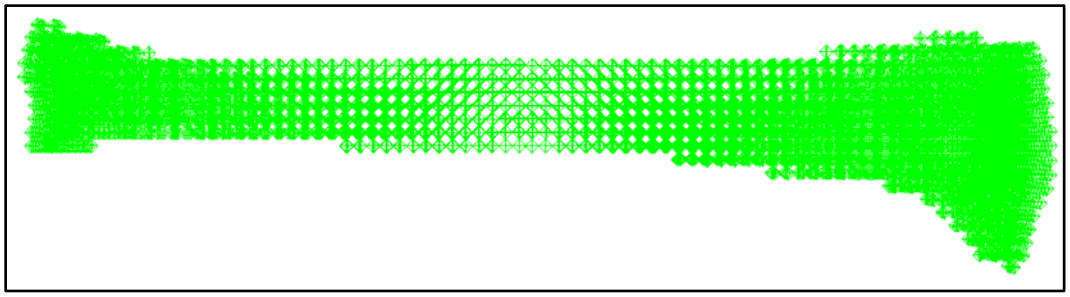

Figure 3.3.1 – Representative model of a lattice encompassing a section of a scanned tibia with a 5 mm voxel pitch and 0.1 mm beam width.

Once the lattice is generated, the program applies boundary conditions, ABAQUS step information, material properties, and exports an input file for the ABAQUS Computational Element Analysis software using a uniquely generated filename for simple post-processing later. Simulated compressive displacements were applied normal to the proximal end of the tibial section to mimic the direction to which natural bone would typically be subject. Although bone is often subject to multiple forces, we focus on the downward force of the torso's weight due to gravity. Using displacement boundary conditions on the vertices that were desired to be loaded keeps consistent applied stress when the number of voxels in the mesh increases, as opposed to applying a concentrated force at each vertex that would scale the total load. The distal end of the tibial section was fully fixed. The program applies the material properties for Polylactic Acid (PLA), a common 3D printable material, which assumes an elastic modulus of 2.79 GPa and a Poisson's ratio of 0.35.

The pitch of the voxels and their beam widths were varied to determine an optimal combination of relative density to effective elastic modulus for the generated lattice structure. Specifically, we compare the effective elastic modulus of a lattice given the pitch, which determines the number of voxels, and the beam width. To determine this optimal combination, a program was written to iterate through 13 different pitches (3, 4, 5, 6, 7, 8, 9, 10, 13, 16, 19, 22, and 25mm) and 9 beam widths (0.1, 0.25, 0.50, 0.75, 1.00, 1.25, 1.50, 1.75, and 2.00 mm) to generate ABAQUS input files with each combination of parameters. The pitches were chosen to give more data points to target a wide distribution of simulated voxel densities. The simulations were run with 4 GB of available memory allocated and parallelized with 4 CPU cores. Simulation run times varied based on the number of voxels in the lattice structure but did not exceed 120 seconds for a 16381-voxel lattice. The stresses evident in a 4062-voxel lattice after 1 mm compressive displacement are shown in *Figure 3.3.2.* Deformation in the figure is exaggerated to represent displacement due to stresses.

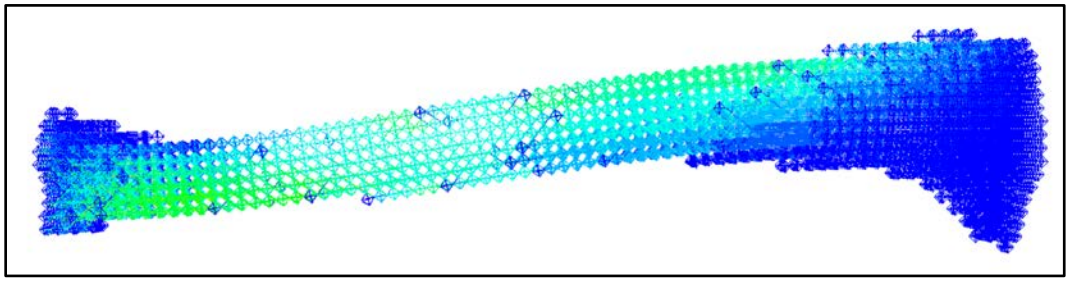

Figure 3.3.2 – Representative model of a stressed lattice after a compressive displacement of 1mm. This model uses a 5 mm voxel pitch and 0.1 mm beam width.

A program was written to optimize the extraction of results from each simulation to a single file. The maximum von Mises stress and its corresponding element number were extracted from the output file of the simulation. The von Mises stress was chosen since it is commonly used to predict when a material will reach the yield point based on the structural stress exceeding that of the material's yield strength (Nisbett and G. Budynas,

2015). The voxel pitch, beam width, and displacement were each extracted from the output file based on the automatically generated filename. The number of voxels for a given pitch was outputted and recorded upon initial file generation. We compared the resulting stresses to the fracture strength of bone that was determined from the literature as well as the average ultimate strength of PLA. The effective elastic modulus of the lattice was determined based on the stress and displacement, for better comparison against other materials and the various iterations of lattice parameters. Additional simulations were performed using the material properties of a titanium alloy, Ti-6Al-4V, which is commonly used for orthopedic implants. Further simulations were performed with the properties of an injection mold thermoplastic, Ultem 2200, already tested with voxel lattices in aerospace applications. The titanium alloy assumes an elastic modulus of 113.8 GPa and a Poisson's ratio of 0.342. The injection mold thermoplastic assumes an elastic modulus of 6.89 GPa and a Poisson's ratio of 0.38.

3.4 – Verification of Computational Results

A printable lattice specimen emulating a cylindrical cross-section was generated using the Rhino 3D mesh editing software based on a voxel of pitch 8 mm and beam width of 1 mm. The structure has a diameter of 40 mm and a height of 40 mm. Four lattice specimens were 3D printed at a resolution of 0.1 mm using Fused Deposition Modeling (FDM) printing methods with a Prusa i3 MK3S. Due to limitations of 3D printing technology available to the researchers, thin strands of printing artifacts were apparent in the printed lattice as seen in the leftmost picture of *Figure 3.4.1*. The mass of each printed lattice was recorded, and its solid volume determined using the volume tool in Rhino 3D. These specimens were mechanically tested in compression using an ADMET eXpert 8602

Biaxial Testing Machine (Norwood, MA) to compare to simulated models. The setup of a lattice specimen in the ADMET is shown in the middle picture of *Figure 3.4.1*. Initially, the ADMET was set to displacement control until 50% strain of the structure to ensure failure, but the compressive strain was modified to 25% for later trials. The rightmost picture of *Figure 3.4.1* shows a lattice specimen after a 25% strain was applied. It was determined that compression up to 10% strain of the structure was needed to display the linear elastic region and peak stress of the structure. A displacement rate of 4 mm/min was chosen to ensure a strain rate of 0.001666 mm/mm/s to be consistent with prior unpublished NASA research on voxel lattice compression. The specimen was displaced until failure to acquire a stress-strain curve. Using this curve, we determined the effective elastic modulus of the printed structure.

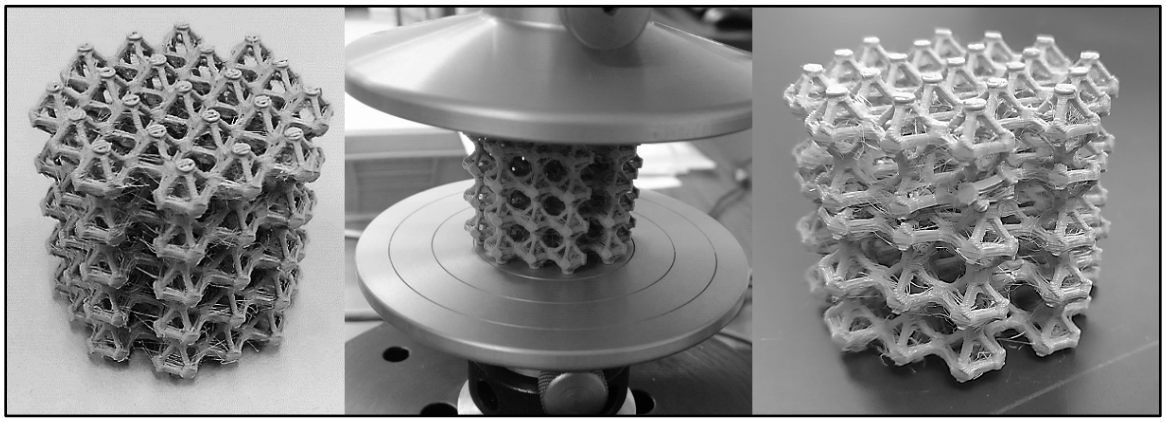

Figure 3.4.1 – (Left) 3D printed cylindrical lattice specimen, (Middle) Printed Lattice Experimental Setup, (Right) Visible fracture and deformation on printed lattice after 25% strain applied.

In conjunction, a comparable lattice was digitally generated and simulated with the same parameters as the 3D printed specimen, using the material properties of PLA, to ensure a direct correlation between the physical experiment and the computational simulation. *Figure 3.4.2* depicts the simulated comparable lattice and its affiliated stress locations after a displacement of 1 mm, consistent with the displacement used for prior simulations in this study. The peak stress for other strains can be extrapolated due to the linearity assumption of the stress and displacement in ABAQUS. The effective elastic modulus was determined for the computational simulation and compared to the experimental results.

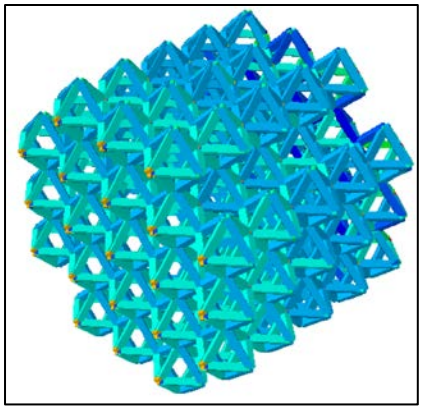

Figure 3.4.2 – Digital cylindrical lattice specimen simulated to 2.5% strain or 1mm displacement.

3.5 –Emulation of Osteosarcoma Surgical Intervention

This study targets the emulation of a surgical intervention on the proximal portion of the osteosarcoma afflicted tibia. The 3D scan of the cadaveric tibia was imported into Meshmixer, a mesh editing software, where the inflate and draw brushes from the 3D sculpt function was used to artificially generate a tumor. The tumor is positioned inferior and lateral to the tibial tuberosity. The mesh was exported to Autodesk Fusion 360 to reduce the number of mesh faces and be compatible with Fusion's Mesh to BRep feature. This feature converted the mesh into a solid model.

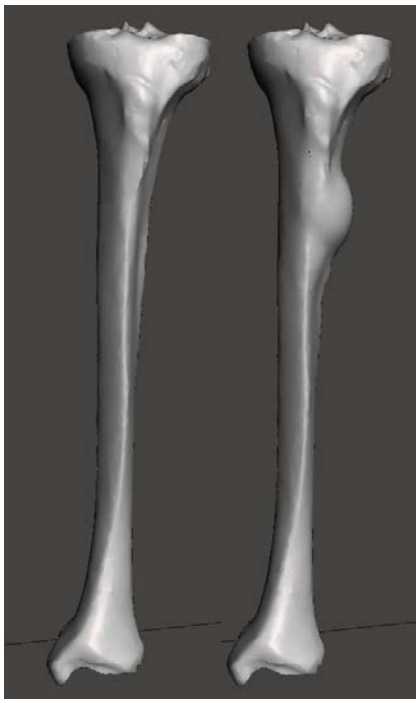

Figure 3.5.1 – Left: Original tibia scan, Right: Modified tibia with artificial osteosarcoma

Radiology images of afflicted long bones from literature were used to adequately gauge the typical size and depth of tumor for resection (McCarthy and Frassica, 2014). The afflicted region was first isolated with 100 mm long section of the proximal tibia. In Fusion 360, a sketch plane was formed to emulate the path of an incision. The sketch was extruded to generate a surface with which to cut the tibial solid model. Once the tumor was separated, an accurate bounding shape of the remaining section was needed to determine the size of the implant.

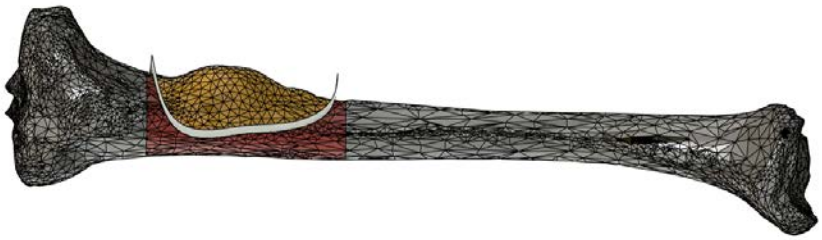

Figure 3.5.2 – Incision surface used to cut tumor (yellow) from tibial section (red).

Temporarily ignoring the tibial section previously isolated, an estimation of the outer body was formed using the loft function between the disjoined portion containing the proximal epiphysis/metaphysis and the portions containing the distal diaphysis. The incision surface was then used on the outer body estimation to create a body representing the implantable region. The outer surface of this body was converted to a thin surface geometry to use later as an incision surface. The surface was also thickened to 0.25 mm, chosen to be thinner than the struts of the lattice, to form a thin outer protective shell for the interior implant design.

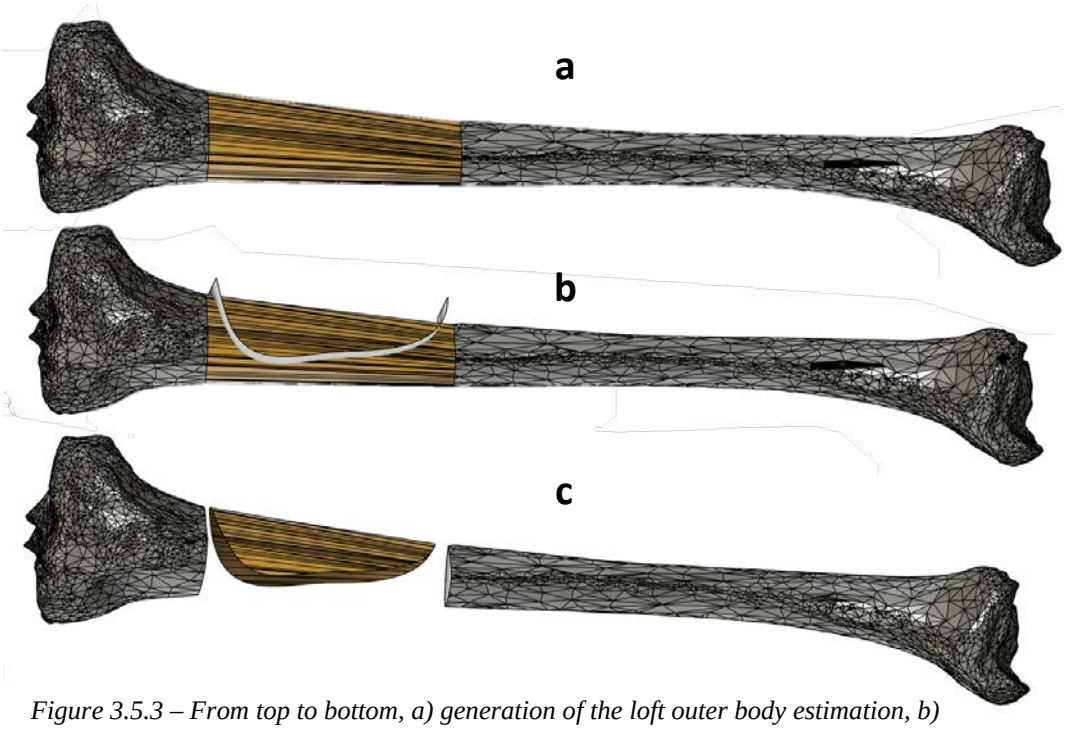

Figure 3.5.3 – From top to bottom, a) generation of the loft outer body estimation, b) using incision surface to create implantable region, c) thin outer protective shell for implant

3.6- Implementation of Custom Lattice as an Implant

For use as an implant, the octahedron lattice geometry must ideally conform to the boundaries of the bone in order to not interfere with surrounding tissue. Each implant must have its interior lattice geometry customized to match to the needs of the patient and the conditions of the surgery. A single voxel was generated using the Rhino 3D mesh editing software based on a voxel of pitch 8 mm and beam width of 1 mm and was converted to a solid BRep geometry. This voxel imported into Fusion 360 for assembly into a workable lattice structure due to computational constraints when working with complex BRep structures in Rhino 3D. In Fusion, the voxel was patterned and merged into a lattice 8 voxels wide, 6 voxels in length, and 15 voxels in height. The initial size of the lattice is customized to exceed the boundaries of the implant to minimize the total number of the voxels thus maximizing the computational efficiency of future steps.

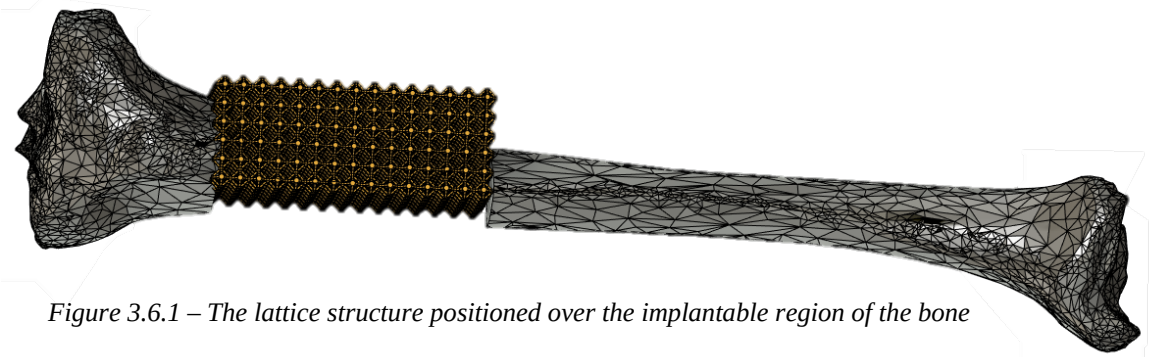

Figure 3.6.1 – The lattice structure positioned over the implantable region of the bone

The center of the lattice structure was positioned to match the center point of the implantable region's bounding box such that the implantable region is completely contained within the lattice as shown in *Figure 3.6.1*. The design of a lattice implant intends for multitude of lattice surfaces to be in contact with surfaces of the bone. Due to the irregular shape of the implantable region, restricting the design to the use of full voxels would minimize the number of contact points and intuitively increase the stress distribution

on voxel outliers. It is therefore appropriate to split full voxels that intersect with the boundary to contour the lattice such that there is more contacting surface area. The current iteration of this design opts for the use of bone cement as opposed to screws or pegs to adhere the lattice to the interior surfaces of the bone. Thus, overly thin geometries that result from the lattice contouring will be coated in cement such that individual struts will be fixed to the cement layer, connecting the rest of the lattice structure to the bone.

The incision surface used to resect the tumor in *Figure 3.5.2* was again employed to split the lattice structure to contour to the interior of the resected bone as shown in *Figure 3.6.2*. The resulting bodies outside of the incision surface or disconnected from the inner lattice were removed.

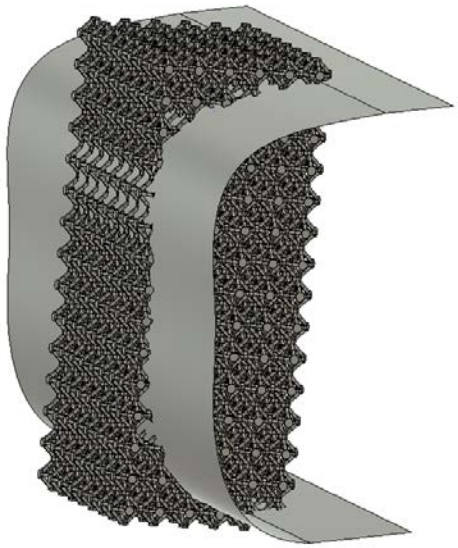

Figure 3.6.2 – Using incision surface to split the lattice body to contour to the resected bone.

From the outer body of the implantable region, the incision surface that was generated in *Chapter 3.5* was utilized to contour the environment facing surfaces of the lattice through an additional split of the lattice body. This split shapes the lattice to the bounds of loft operation for the estimation of the bone's outer body.

Figure 3.6.3 – Using incision surface to split the lattice body to contour to the estimation of the bone's outer body.

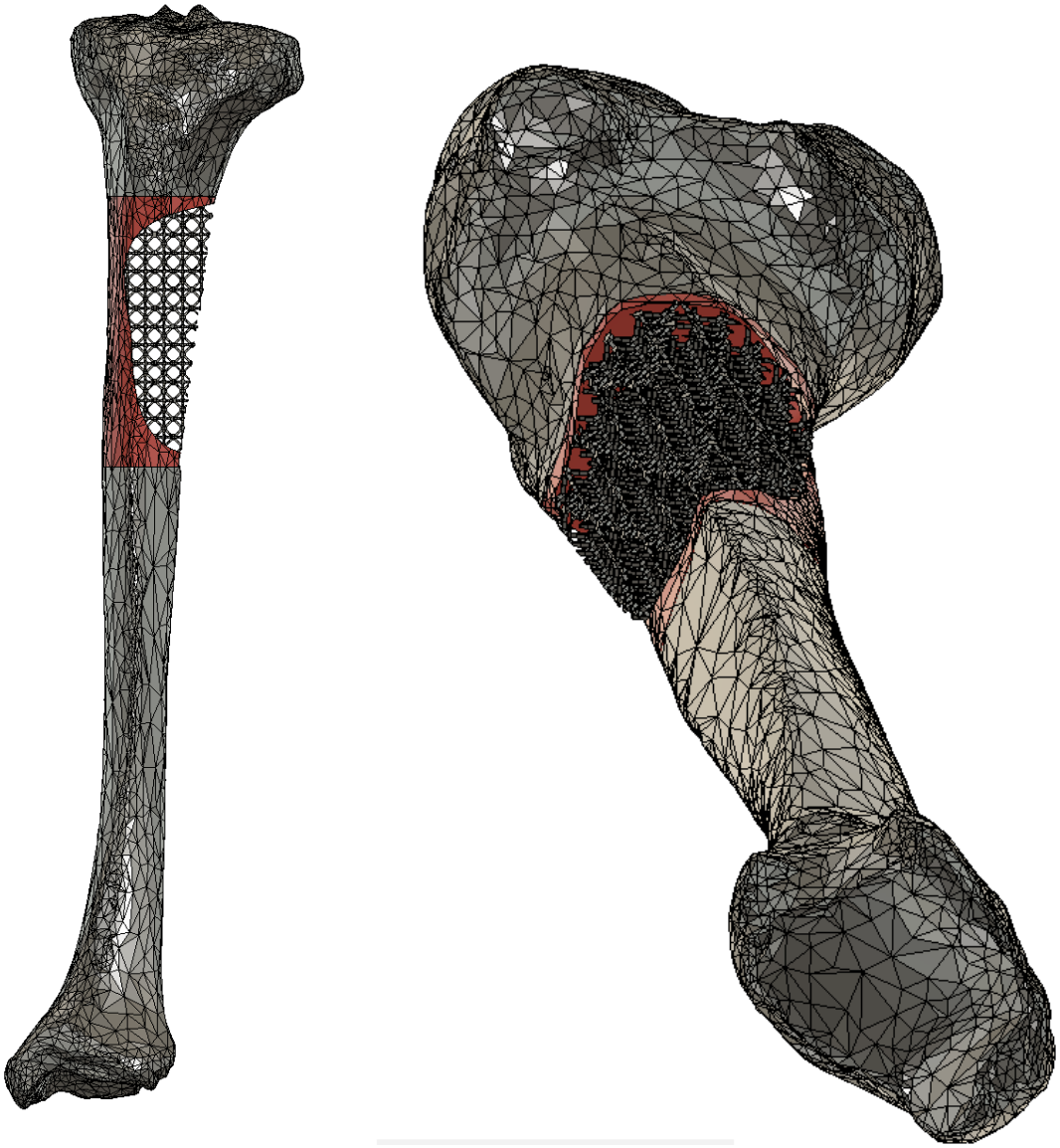

Figure 3.6.4 – The contoured lattice structure fit within the confines of the bone. Anterior view (left) and Perspective view (right) of the lattice bone implementation

The resulting contoured lattice structure demonstrated within the confines of the bone is depicted in *Figure 3.6.4*. As shown in *Figure 3.6.5*, the resulting lattice is geometrically integrated with the thin outer protective shell from *Chapter 3.5* so it can be 3D printed homogeneously with the lattice implant design,.

Figure 3.6.5 – The contoured lattice structure geometrically integrated with the outer protective shell

3.7- Estimation of Normal Tibial Behavior

The unmodified 3D scan of the cadaveric tibia was converted into a workable solid model in Fusion 360 in the same process as described for the osteosarcoma model in *Chapter 3.5.* A 100 mm section was split at the same locations and exported to ABAQUS. Since the origin of the model was a scanned mesh, the solid model contained many small faces that complicated the ABAQUS meshing process. The virtual topology feature present in ABAQUS was used to combine all faces and edges in the model except for the edges at the top and bottom boundary. The model was duplicated to consider compare two models of the normal tibial behavior with the same constraints and loading conditions.

The first model assumed tibial behavior as a closed, homogenous solid. The model was partitioned into cells along the XZ and YZ planes where the length of the model was constrained in the Z direction. A linear hexagonal mesh (element type C3D8R) with a seed size of 2.5 was used. The second model assumed tibial behavior as a membrane-like shell with a given thickness. The model was first converted to a shell from a solid in ABAQUS's part module and the top and bottom faces were removed leaving only the outer surface of the tibia. The second model was also partitioned into faces along XZ and YZ planes. The normal directions of the faces were inverted such that the material thickness is calculated facing inward. A mesh was constructed out of linear quadrilateral-dominated (S4R) elements with an element size of 2.5 mm. An average cortical bone thickness of 3.5 mm was assumed (Patterson et al., 2016). A shell thickness of 2.5 mm was also simulated. Both models used a base material with an elastic modulus of 14.8 GPa, a Poisson's ratio of 0.35, and a density of 1.86 g/cm^3 (Li and Aspden, 1997).

Constrained nodes were created at the locations where the proximal and distal articular surfaces would be to emulate the boundary effects on the tibial section. The proximal node was generated 60 mm from the center of the top surface of the section. The distal node was set 225 mm from the bottom surface. Coupling constraints fully connected the nodes to the top and bottom surfaces in the case of the solid model. The shell model was fully constrained by its top and bottom edges. The bottom node was fully fixed in place. Two different loading conditions were simulated on the top node to allow conclusions regarding the normal deformation behavior of the tibia under body-weight load. The top node was loaded with a concentrated compressive force of 2000 N. This force was estimated based on the average body weight of 180 lbs among American adults in 2016 with a factor of safety of 2.5 as reported by the National Center for Health Statistics (Fryar et al., 2018). A compressive force of 1000 N was tested for a factor of safety of 1.25.

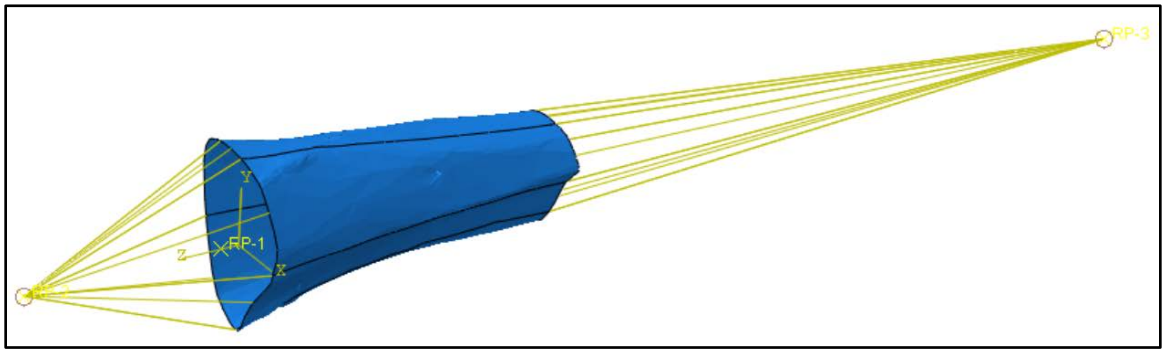

Figure 3.7.1 – The coupling constraints on the top and bottom edges of the shelled model of the normal tibial section.

3.8 Analysis of Lattice Implant

Validation of the implant design was performed using the ABAQUS Finite Element Analysis software. The solid geometry of the 100 mm resected tibial section, the contoured lattice structure, and the outer protective shell were imported into ABAQUS as parts. A modification of the lattice with a thin shell located at the bone interface was also imported. The shell at the interface was generated by thickening the incision surface for the resected tumor and cutting the result with the incision surface for the bone's outer body. The thickness of this thin shell is 0.5 mm from the incision surface into the lattice. The lattice was the adjusted with an additional body split using a copy of the incision surface offset 0.3 mm to overlap with the lattice. This process removed small artifacts otherwise apparent during any Boolean combinations with the shell. The shell was integrated with the geometry of the lattice in order to simplify the simulated interaction with the resected bone. The resulting implant was positioned with precise contact between the interior of the resected tibia and shell.

ABAQUS's virtual topology feature was used to combine small faces and redundant edges on the lattice implant to improve mesh efficiency by reducing import artifacts. This functionality was also used to minimize faces and edges on the resected tibial section, allowing it to be meshed with linear hexagonal swept elements (C3D8R) and a seed size of 2.5. The bone was modeled as a homogeneous solid with an elastic modulus of 14.8 GPa, an assumed Poisson's ratio of 0.35, and a density of 1.86 g/cm^3. The lattice implant was modeled as a homogeneous solid with the properties of PLA: an elastic modulus of 2.78 GPa, Poisson's ratio of 0.35, and a density of 1.24 g/cm^3. The implant was meshed with quadratic tetrahedral elements (C3D10) with a seed size of 2.4.

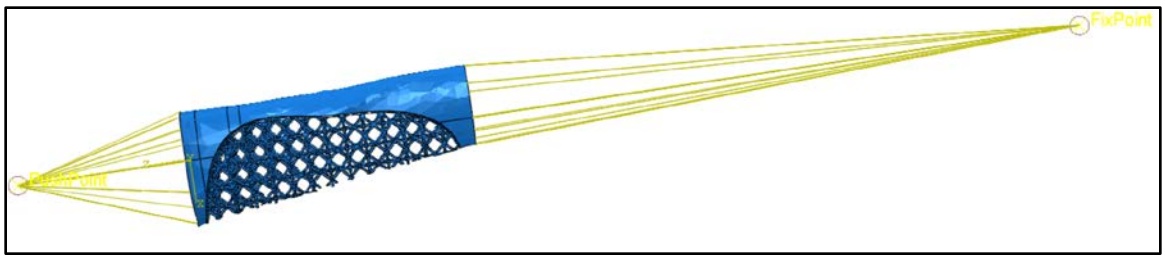

Figure 3.8.1 – The coupling constraints on the top and bottom edges of the shelled model of the normal tibial section.

The constraints and loading conditions followed those used in *Chapter 3.7* for the normal tibial section. Coupling constraints were associated with the top and bottom surfaces of the resected tibia. A general contact interaction was used to define the behavior between the lattice implant and the resected tibia. The normal behavior was defined as hard contact (no overlap) pressure-overclosure formulation without separation and the tangential behavior was defined with a rough (no-slip) frictional formulation. This interaction simulated the implant being fixed to the bone to demonstrate the stress distribution throughout the implant. The distal constraint node was fully fixed. Three models of the proximal constraint node loading conditions were simulated. Two models were defined as compressive concentrated forces of 2000 N and 1000 N as a direct comparison to the loading conditions of the normal tibia in *Chapter 3.7*. Additionally, a compressive displacement on the top node of 0.5 mm was tested, because it would allow conclusions comparing the stress distribution beyond deformations seen in the body-weight loading conditions of the normal tibia in *Chapter 3.7*.

A model of the resected tibial section without the lattice implant was simulated as a comparison to determine whether the lattice offloads stress and reduces maximum axial deformation from the resected bone. The same constraints, geometry, mesh, and element types from the integrated lattice simulation were employed without contact interactions or the lattice geometry to simulate the resected section under 2000 N of loading.

3.9 Physical Representation of Lattice Implant

The lattice structure with the integrated outer shell was manufactured in PLA using fused filament fabrication with a Prusa Mini 3D Printer. The resected tibia and removed tumor were printed in sections separating the proximal epiphysis, the resected section, the distal diaphysis, and the distal epiphysis. The sections were adhered together with cyanoacrylate except for the removed tumor.

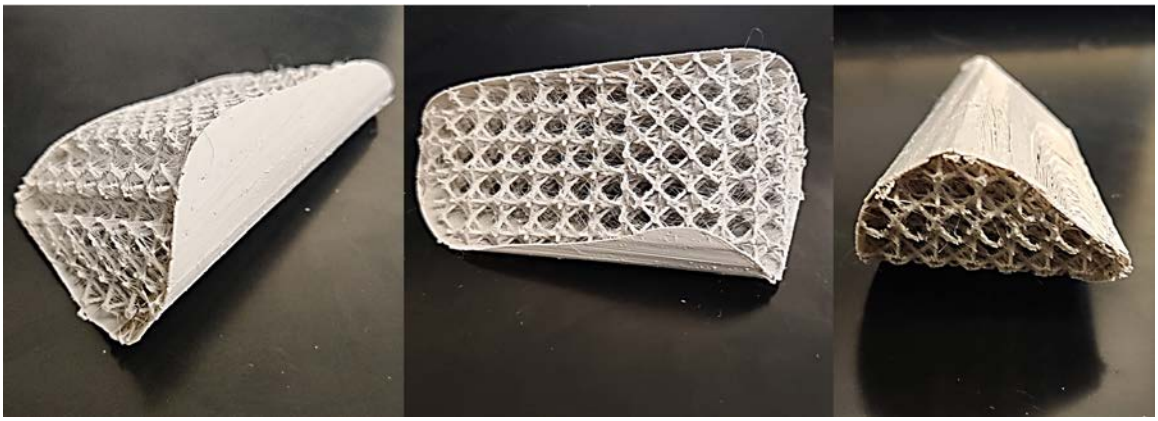

Figure 3.9.1 – Views of printed lattice implant: (Left) Perspective view, (Middle) Medial view, (Right) Superior View

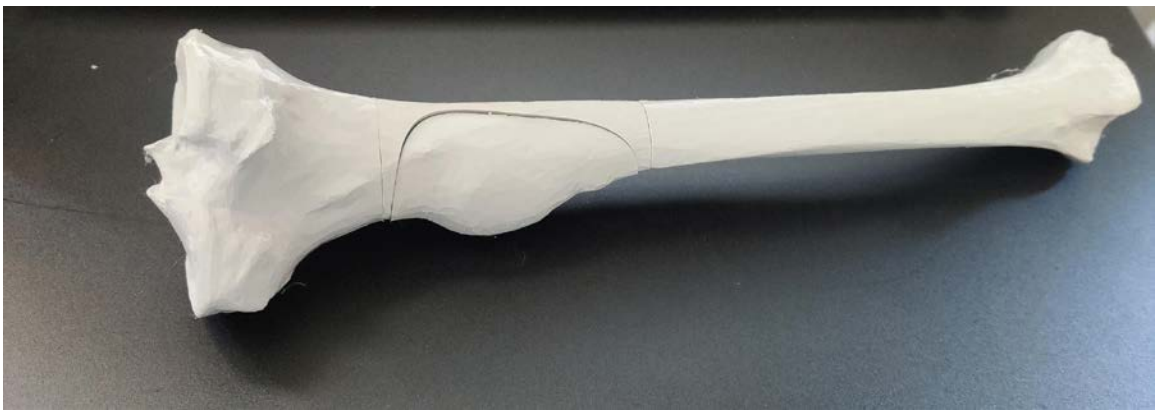

Figure 3.9.2 – Printed tibial specimen with detachable osteosarcoma.

Chapter 4: Results

4.1 – Assumption of Linearity

Figure 4.1 depicts the relationship between voxel pitch and the number of voxels the program generates. The change in the number of voxels present in the structure between 3 mm and 5 mm is greater than the change between 5mm and 7 mm voxel pitches. The number of voxels asymptotically converges when voxel pitch is greater than 10 mm.

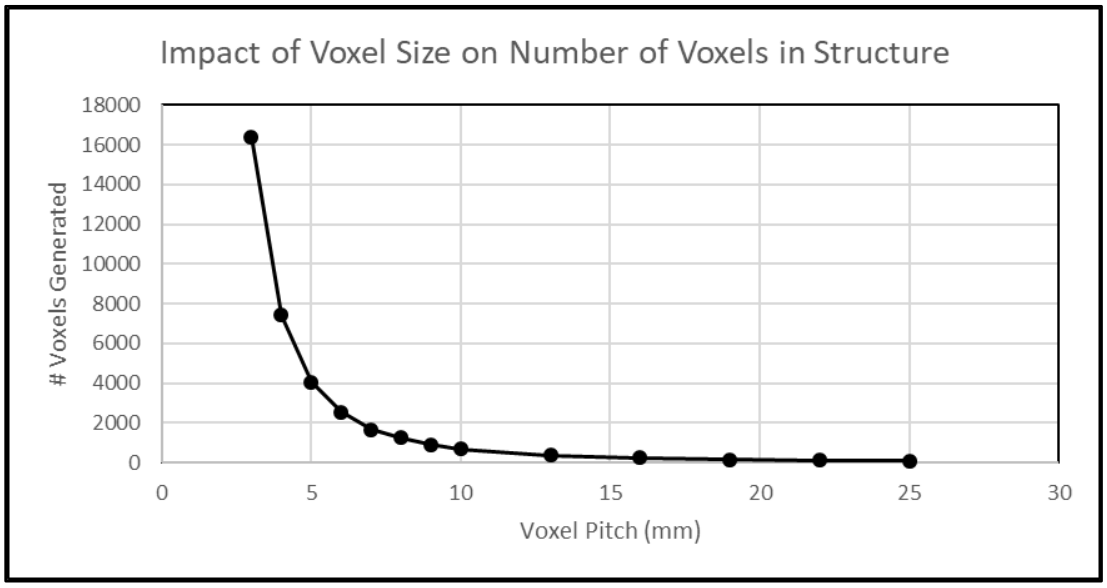

Figure 4.1.1 – Graph showing the exponential increase of the number of voxels as voxel pitch decreases

Table 4.1.2 shows the resulting stresses and associated beam number of sample lattices with 7- and 10-mm voxel pitches tested at 1 mm and 10 mm displacements.

Verification of Linearity Test					
Voxel Size	# of Voxels	Beam Width (mm)	Displacement (mm)	Stress (MPa)	Beam Number
10	682	1.00	1	18.55	16866
10	682	1.00	10	185.5	16866
7	1676	1.00	1	25.37	46350
7	1676	1.00	10	253.7	46350

Table 4.1.2 – Table showing maximum Von Mises stress linearly increasing as compressive displacement increases for voxel pitches of 7- and 10-mm.

4.2 – Maximum Stress Present in Lattice

Table 4.2.1 shows the resulting maximum Von Mises stress present in the lattice given a voxel pitch and beam width combination. *Figure 4.2.2* helps visualize the trends of each beam width as voxel pitch changes. Stress increases as beam width increases and lattices with voxel pitches under 8 mm have higher maximum stresses than those over 8 mm.

Maximum Von Mises Stress (MPa) in Lattice based on Voxel Pitch and Beam Width										
		Beam Width mm								
		0.1	0.25	0.5	0.75	1	1.25	1.5	1.75	2
Voxel Pitch mm (# Voxels)	3 (16381)	13.31	20.03	28.21	32.18	33.47	33.47	33.10	33.08	32.87
	4 (7412)	12.44	16.54	22.90	27.62	30.64	32.44	33.43	33.92	34.09
	5 (4062)	11.30	14.59	20.20	24.75	27.99	30.11	31.41	32.14	32.48
	6 (2544)	10.80	14.41	20.01	24.63	28.09	30.46	31.96	32.81	33.21
	7 (1676)	11.58	14.09	18.26	22.10	25.37	28.00	30.04	31.56	32.68
	8 (1245)	11.26	13.49	17.09	20.54	23.63	26.25	28.41	30.15	31.51
	9 (892)	9.25	10.80	13.48	16.15	18.62	20.78	22.62	24.13	25.36
	10 (682)	8.24	10.10	13.15	16.01	18.55	20.74	22.55	24.02	25.17
	13 (369)	8.44	9.46	11.11	12.79	14.46	16.06	17.58	18.97	20.22
	16 (234)	8.31	9.33	11.21	13.11	14.95	16.69	18.34	19.97	21.42
	19 (151)	6.02	6.71	7.85	8.94	10.00	11.03	12.03	13.04	14.01
	22 (112)	5.78	6.33	7.79	9.19	10.50	11.72	12.84	13.95	14.96
	25 (85)	6.86	7.59	8.78	9.99	11.54	12.99	14.34	15.58	16.73

Table 4.2.1 – Table showing the resulting maximum Von Mises stresses present in the lattice comparing beam width and voxel pitch.

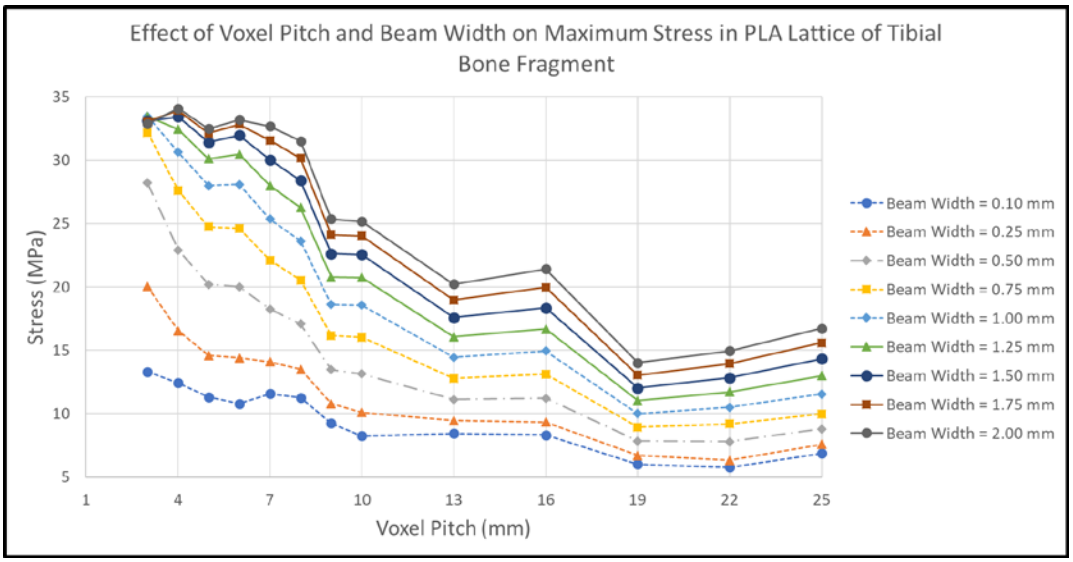

Figure 4.2.2 – Graph showing maximum Von Mises stress present in the tibial bone fragment lattice, as affected by voxel pitch and by beam width.

4.3 – Effective Structural Length of the Simulated Lattice

Table 4.3.1 presents the effective structural length and strain present with 1mm of displacement of the lattice with a given voxel pitch. The average effective strain is 0.270%.

Table of Effective Structural Lengths							
Voxel Pitch (mm)	# Voxels that Divide Length	Total Length Center to Center (mm)	Total Length (mm)	Seperation b/w Nodes along Z Axis (mm)	Moveable Length (mm) Beyond 365 mm	Effective Structural Length (mm)	Effective Strain (%)
3	122	366	369	1.5	1.0	366.5	0.273
4	92	368	372	2.0	1.0	367.0	0.272
5	73	365	370	2.5	0.0	367.5	0.272
6	61	366	372	3.0	1.0	368.0	0.272
7	52	364	371	3.5	2.5	368.5	0.271
8	46	368	376	4.0	3.0	369.0	0.271
9	40	360	369	4.5	4.0	369.5	0.271
10	36	360	370	5.0	0.0	370.0	0.270
13	28	364	377	6.5	5.5	371.5	0.269
16	23	368	384	8.0	3.0	373.0	0.268
19	19	361	380	9.5	5.5	374.5	0.267
22	16	352	374	11.0	9.0	376.0	0.266
25	14	350	375	12.5	10.0	377.5	0.265

Table 4.3.1 – Table showing the effective structural length given a voxel pitch, and the affiliated values that determine it.

4.4 – Effective Elastic Modulus of the Simulated PLA Lattice

The effective elastic modulus of the simulated lattice composing a tibial bone section is shown in *Table 4.4.1* and visualized in *Figure 4.4.2*. The structural modulus of an 8 mm voxel lattice is 11.60 GPa with the PLA material, which is 415% greater than the solid continuum material modulus of PLA.

Effective Elastic Modulus (GPa) of Lattice based on Voxel Pitch and Beam Width										
		Beam Width mm								
		0.1	0.25	0.5	0.75	1	1.25	1.5	1.75	2
Voxel Pitch mm (# Voxels)	3 (16381)	4.87	7.33	10.32	11.78	12.25	12.25	12.11	12.11	12.03
	4 (7412)	4.55	6.05	8.38	10.11	11.21	11.87	12.24	12.41	12.48
	5 (4062)	4.12	5.33	7.37	9.03	10.22	10.99	11.46	11.73	11.86
	6 (2544)	3.95	5.27	7.32	9.01	10.28	11.15	11.70	12.01	12.15
	7 (1676)	4.26	5.18	6.71	8.12	9.32	10.29	11.04	11.60	12.01
	8 (1245)	4.14	4.96	6.29	7.56	8.70	9.66	10.45	11.10	11.60
	9 (892)	3.41	3.99	4.97	5.96	6.87	7.67	8.35	8.90	9.36
	10 (682)	3.01	3.69	4.80	5.84	6.77	7.57	8.23	8.77	9.19
	13 (369)	3.13	3.50	4.12	4.74	5.36	5.95	6.51	7.03	7.49
	16 (234)	3.06	3.43	4.13	4.82	5.50	6.14	6.75	7.35	7.88
	19 (151)	2.23	2.49	2.91	3.31	3.71	4.09	4.46	4.83	5.19
	22 (112)	2.16	2.37	2.91	3.44	3.93	4.38	4.80	5.22	5.60
	25 (85)	2.57	2.85	3.29	3.74	4.33	4.87	5.38	5.84	6.27

Table 4.4.1 – Table showing the effective elastic modulus of the lattice, as affected by voxel pitch and by beam width.

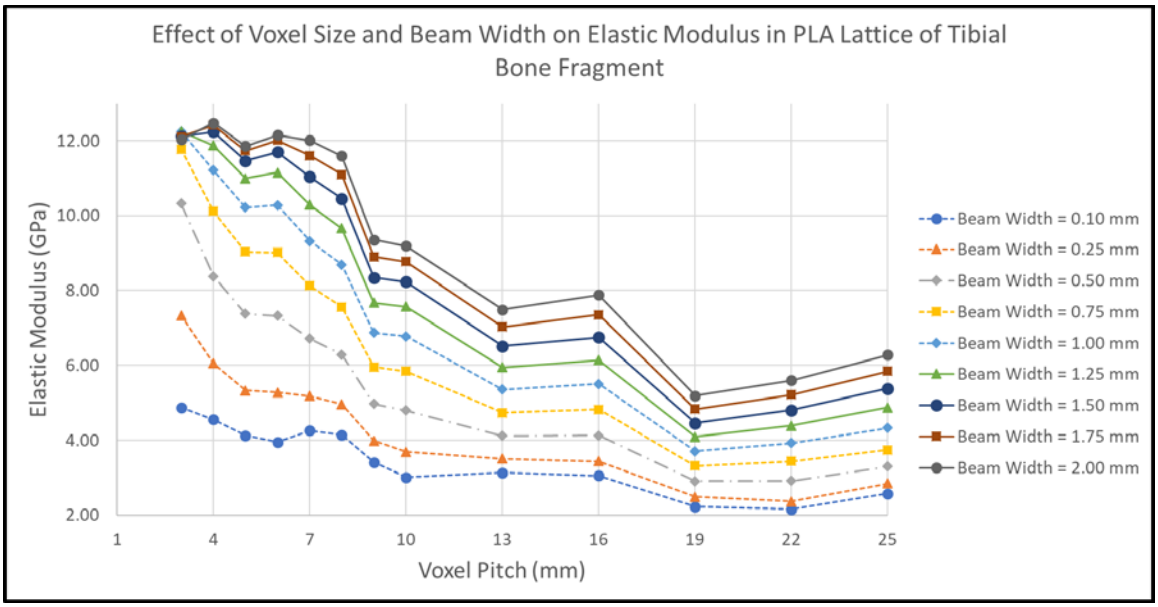

Figure 4.4.2 – Graph showing the relationship between effective elastic moduli of the lattices simulated, as affected by voxel pitch and by beam width.

It is of importance that we consider the exponential relationship between voxel pitch and the number of voxels in the lattice. As such it is of benefit to evaluate the relationship between voxel density and elastic modulus that results from a given beam width. This relationship is explored in *Figures 4.4.3* and *4.4.4.*

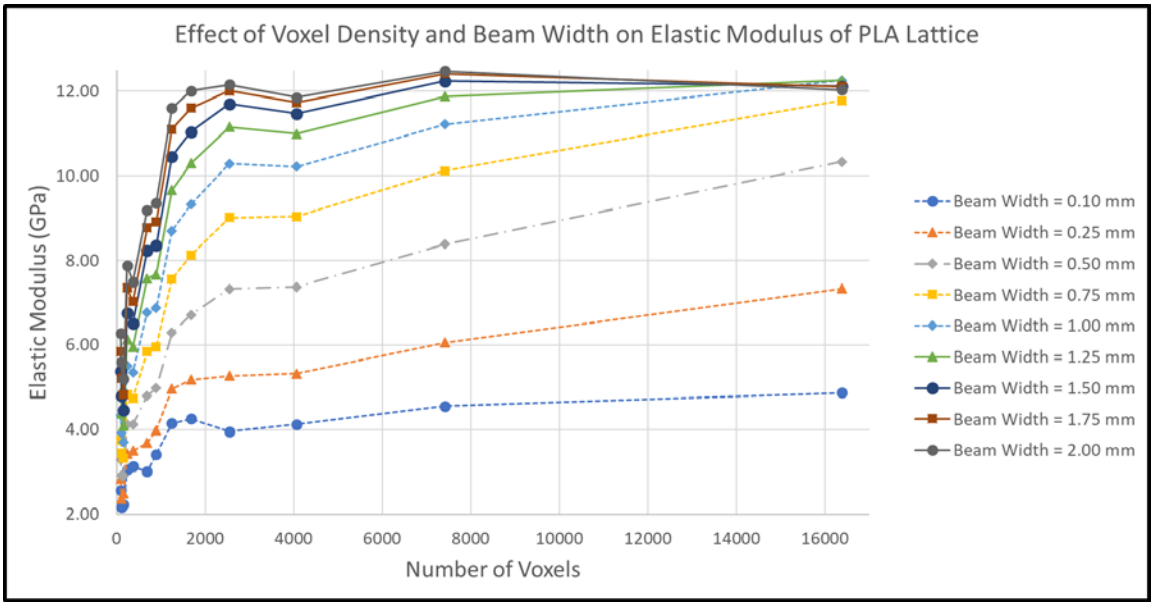

Figure 4.4.3 – Graph showing the relationship between effective elastic moduli of the lattices simulated, as affected by voxel density and by beam width.

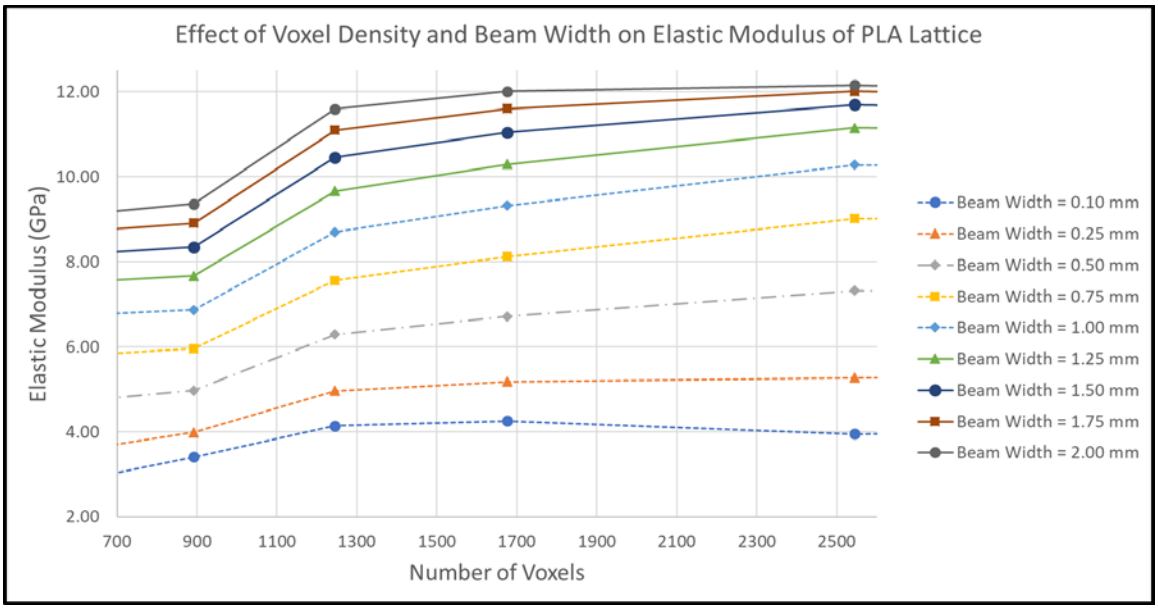

Figure 4.4.4 – Graph zooming in on the behavior of effective elastic moduli of the lattices simulated due to beam width ranging between a voxel pitch of 6 mm (2544 total voxels) and a pitch of 13 mm (369 total voxels).

4.5 –Lattice Simulations using Titanium Alloy

The lattice was simulated with the material properties of the Titanium alloy Ti-6Al-4V, which is commonly used in orthopedic implants (Pobloth et al., 2018). The maximum stress present in an 8 mm voxel pitch lattice is 1288 MPa.

Maximum Von Mises Stress (MPa) in Lattice based on Voxel Pitch and Beam Width										
		Beam Width mm								
		0.1	0.25	0.5	0.75	1	1.25	1.5	1.75	2
Voxel Pitch mm (# Voxels)	3 (16381)	543.6	819	1154	1316	1369	1369	1353	1352	1343
	4 (7412)	507.7	675.9	935.9	1129	1253	1326	1367	1387	1394
	5 (4062)	461.2	595.9	825.5	1012	1144	1231	1285	1314	1328
	6 (2544)	440.9	588.7	818.1	1007	1149	1246	1307	1342	1358
	7 (1676)	472.4	575.2	745.8	903.2	1037	1145	1228	1290	1336
	8 (1245)	459.3	550.8	697.9	839.3	965.5	1073	1161	1232	1288
	9 (892)	377.3	440.9	550.4	659.9	761	849.5	924.4	986.4	1037
	10 (682)	336.3	412.2	537.3	654.4	758.6	848	922.3	982.3	1030
	13 (369)	344.4	385.8	453.7	522.3	590.5	656.4	718.4	775.3	826.6
	16 (234)	338.9	380.7	457.5	535.4	610.6	682.1	750.1	817.1	876.4
	19 (151)	245.5	273.8	320.2	365	408.5	450.7	491.4	533.6	573
	22 (112)	235.6	258.4	318.1	375.6	429.3	479.2	525.1	570.4	611.9
	25 (85)	279.7	309.7	358.5	408.2	471.8	531.2	586.4	637.3	684.1

Table 4.5.1 – For the titanium alloy lattice, table showing the resulting maximum Von Mises stresses present based on beam width and voxel pitch.

Table 4.5.2 and *Figure 4.5.3* display the effective elastic modulus of the simulated lattice molded to a tibial bone section with the material properties of a titanium alloy. Note that the trends for the lattice with titanium is like that of PLA but with a 4086% increase in the magnitude of the modulus. The peak modulus at a pitch of 8 mm is 473.98 GPa.

Effective Elastic Modulus (GPa) of Lattice based on Voxel Pitch and Beam Width										
		Beam Width mm								
		0.1	0.25	0.5	0.75	1	1.25	1.5	1.75	2
Voxel Pitch mm (# Voxels)	3 (16381)	198.96	299.75	422.36	481.66	501.05	501.05	495.20	494.83	491.54
	4 (7412)	185.82	247.38	342.54	413.21	458.60	485.32	500.32	507.64	510.20
	5 (4062)	168.34	217.50	301.31	369.38	417.56	449.32	469.03	479.61	484.72
	6 (2544)	161.37	215.46	299.42	368.56	420.53	456.04	478.36	491.17	497.03
	7 (1676)	173.61	211.39	274.08	331.93	381.10	420.79	451.29	474.08	490.98
	8 (1245)	169.02	202.69	256.83	308.86	355.30	394.86	427.25	453.38	473.98
	9 (892)	139.22	162.69	203.10	243.50	280.81	313.47	341.10	363.98	382.65
	10 (682)	122.75	150.45	196.11	238.86	276.89	309.52	336.64	358.54	375.95
	13 (369)	127.60	142.94	168.10	193.51	218.78	243.20	266.17	287.25	306.26
	16 (234)	124.72	140.10	168.36	197.03	224.70	251.01	276.04	300.69	322.52
	19 (151)	90.96	101.44	118.63	135.23	151.35	166.98	182.06	197.70	212.30
	22 (112)	88.11	96.64	118.97	140.47	160.56	179.22	196.39	213.33	228.85
	25 (85)	104.89	116.14	134.44	153.08	176.93	199.20	219.90	238.99	256.54

Table 4.5.2 – For the titanium alloy lattice, table showing the resulting effective elastic modulus based on beam width and voxel pitch.

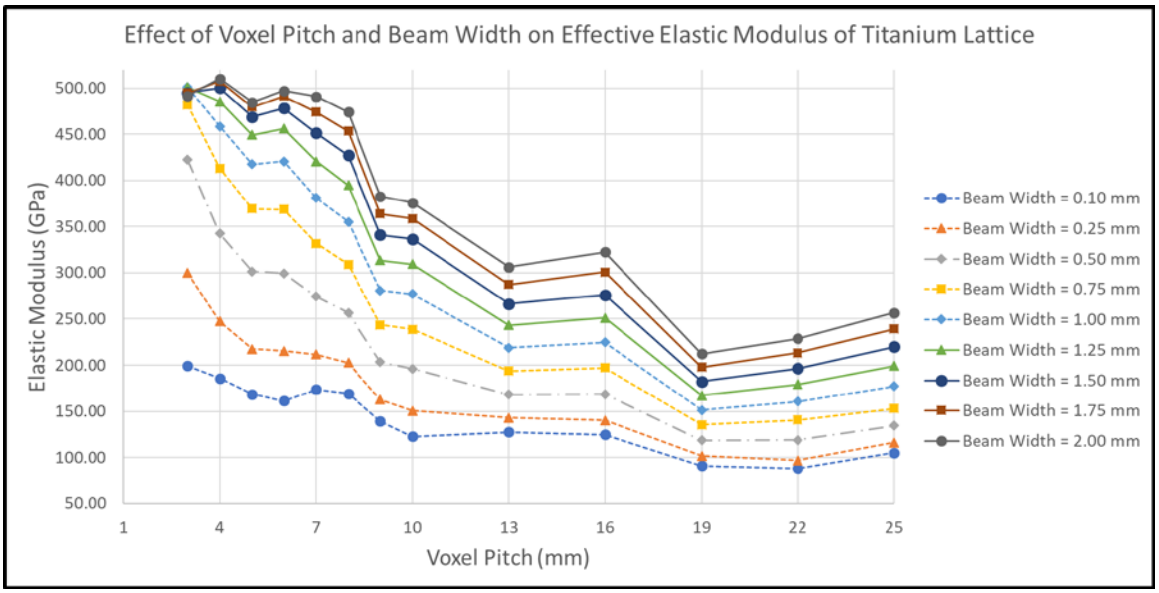

Figure 4.5.3 – For the titanium alloy lattice, graph visualizing the resulting effective elastic modulus based on beam width and voxel pitch.

4.6 – Lattice Simulations using Ultem 2200 Thermoplastic

The lattice was simulated with the material properties of the injection mold thermoplastic Ultem 2200, which has been tested for voxel lattices in aerospace applications (Cramer et al., 2019). The peak stress with an 8 mm voxel pitch is 76.06 MPa.

Maximum Von Mises Stress (MPa) in Lattice based on Voxel Pitch and Beam Width										
		Beam Width mm								
		0.1	0.25	0.5	0.75	1	1.25	1.5	1.75	2
Voxel Pitch mm (# Voxels)	3 (16381)	32.23	48.32	67.92	77.45	80.57	80.62	79.95	79.92	79.41
	4 (7412)	30.23	39.95	55.31	66.64	73.94	78.27	80.69	81.88	82.31
	5 (4062)	27.47	35.33	48.76	59.67	67.46	72.58	75.71	77.47	78.31
	6 (2544)	26.23	34.86	48.27	59.33	67.61	73.32	76.93	79	79.95
	7 (1676)	28.16	34.18	44.18	53.41	61.27	67.59	72.49	76.17	78.87
	8 (1245)	27.38	32.74	41.37	49.67	57.07	63.38	68.58	72.76	76.06
	9 (892)	22.5	26.23	32.65	39.06	44.98	50.18	54.59	58.23	61.21
	10 (682)	20.04	24.47	31.77	38.62	44.71	49.94	54.29	57.81	60.58
	13 (369)	20.56	22.98	26.96	30.98	34.97	38.83	42.46	45.8	48.8
	16 (234)	20.23	22.68	27.17	31.73	36.14	40.33	44.25	47.99	51.46
	19 (151)	14.65	16.31	19.03	21.65	24.2	26.67	29.05	31.37	33.67
	22 (112)	14.06	15.36	18.83	22.18	25.32	28.23	30.91	33.56	35.99
	25 (85)	16.69	18.45	21.31	24.09	27.8	31.28	34.51	37.49	40.23

Table 4.6.1 – For the Ultem 2200 lattice, table showing the resulting maximum Von Mises stresses present based on beam width and voxel pitch.

Table 4.6.2 and *Figure 4.6.3* display the effective elastic modulus of the simulated lattice molded to a tibial bone section with the material properties of Ultem 2200 thermoplastic. Note that the trends for the lattice with this thermoplastic is like that of PLA but with a 241% increase in the magnitude of the modulus. At higher beam widths greater than 1.5 mm and voxel pitches less than 8mm, the modulus is within 5 GPa of the highest simulated elastic modulus. The peak modulus with an 8mm pitch is 27.99 GPa.

Effective Elastic Modulus (GPa) of Lattice based on Voxel Pitch and Beam Width										
		Beam Width mm								
		0.1	0.25	0.5	0.75	1	1.25	1.5	1.75	2
Voxel Pitch mm (# Voxels)	3 (16381)	11.80	17.69	24.86	28.35	29.49	29.51	29.26	29.25	29.06
	4 (7412)	11.06	14.62	20.24	24.39	27.06	28.65	29.53	29.97	30.13
	5 (4062)	10.03	12.90	17.80	21.78	24.62	26.49	27.63	28.28	28.58
	6 (2544)	9.60	12.76	17.67	21.71	24.75	26.84	28.16	28.91	29.26
	7 (1676)	10.35	12.56	16.24	19.63	22.52	24.84	26.64	27.99	28.98
	8 (1245)	10.08	12.05	15.22	18.28	21.00	23.32	25.24	26.78	27.99
	9 (892)	8.30	9.68	12.05	14.41	16.60	18.52	20.14	21.49	22.59
	10 (682)	7.31	8.93	11.60	14.10	16.32	18.23	19.82	21.10	22.11
	13 (369)	7.62	8.51	9.99	11.48	12.96	14.39	15.73	16.97	18.08
	16 (234)	7.44	8.35	10.00	11.68	13.30	14.84	16.28	17.66	18.94
	19 (151)	5.43	6.04	7.05	8.02	8.97	9.88	10.76	11.62	12.47
	22 (112)	5.26	5.74	7.04	8.30	9.47	10.56	11.56	12.55	13.46
	25 (85)	6.26	6.92	7.99	9.03	10.43	11.73	12.94	14.06	15.09

Table 4.6.2 – For the Ultem 2200 lattice, a table showing the resulting effective elastic modulus based on beam width and voxel pitch.

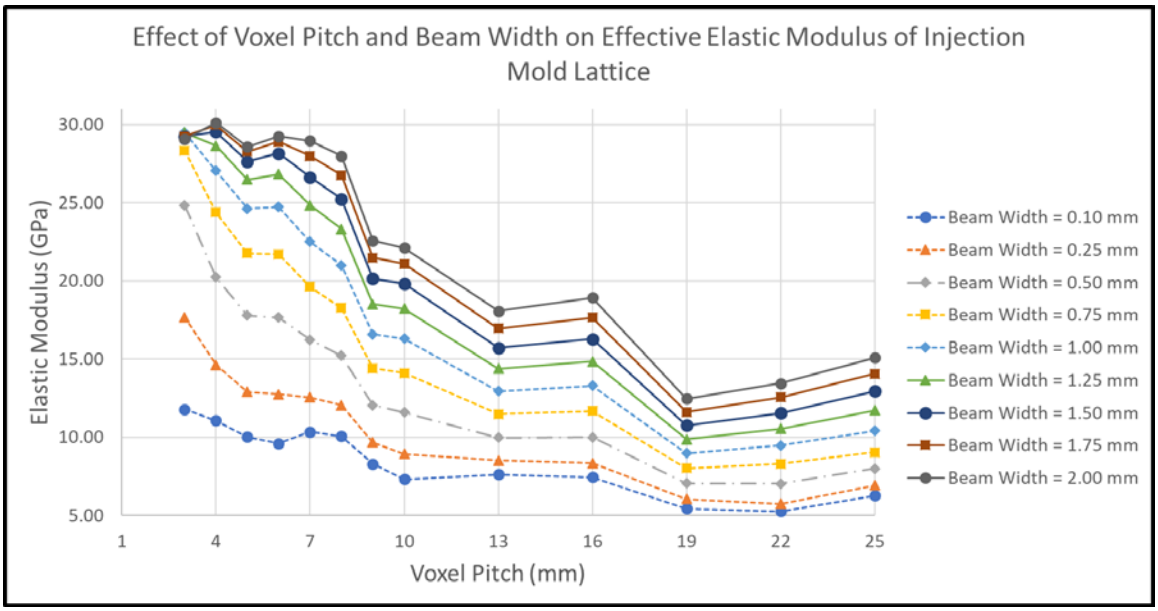

Figure 4.6.3 – For the Ultem 2200 lattice, graph visualizing the resulting effective elastic modulus based on beam width and voxel pitch.

Figure 4.6.4 uses a beam width of 2 mm for visualization of the effective elastic modulus with different material constructions simulated. The graph uses a log scale to depict the consistent trend regardless of material. The scaling effect of using a different construction material in the simulation is evident.

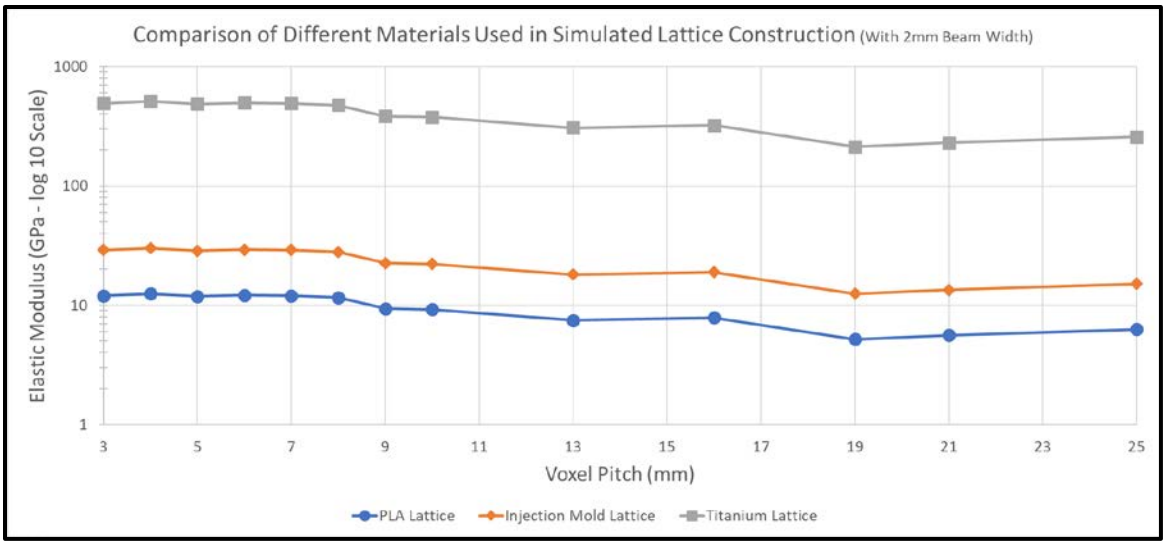

Figure 4.6.4 – Comparison of the resulting effective elastic modulus with different material constructions, different voxel pitches, and a beam width of 2 mm.

4.7 – Experimental Testing of Cylindrical Lattice Section

A cylindrical section, composed of a lattice with 8 mm pitch and 1 mm beam width, was 3D printed four times and mechanically compressed. The results were then compared to a simulated model of the specimen with the same parameters as shown in *Table 4.7.1*. Note that there exists a 7-12 % error between the ratio of stresses experimentally and the linear ratio of stresses assumed in the simulation. The experimental moduli have an average of 0.57 ± 0.047 GPa. The experimental moduli are 28.16% ± 2.33% of the simulated effective modulus.

Comparison of Experimental to Computational Results													
Specimen Number	Volume (mm^3)	Mass (g)	Height (mm)	Area (mm^2)	Maximum Load (N)	Max Load Position (mm)	Pt 1 / Position @ 40% Peak Stress (mm)	Pt 2 / Position @ 50% Peak Stress (mm)	Stress (MPa) @ Pt 1	Stress (MPa) @ Pt 2	Modulus (GPa)	Ratio of Stresses	% Error of Linearity
Sim	2630.10	7.34	40	65.75	N/A	N/A	1.00	1.25	50.54	63.17	2.02	1.25	N/A
2	2630.10	8.38	40	65.75	1588.22	2.27	0.91	1.14	10.18	13.72	0.62	1.35	7.24
3	2630.10	8.39	40	65.75	1649.98	2.49	1.00	1.25	10.44	14.22	0.61	1.36	8.27
4	2630.10	8.34	40	65.75	1519.93	2.50	1.00	1.25	9.56	12.87	0.53	1.35	7.16
5	2630.10	8.29	40	65.75	1496.92	2.78	1.11	1.39	8.56	12.14	0.52	1.42	11.89

Table 4.7.1 – Experimental results 2-5 and comparative simulated result "Sim"

Figure 4.7.2 depicts the qualitative results of the lattice compression test. Specimen 2 was taken to 50% strain, specimen 3 to 13% strain, and specimens 4 and 5 to 25% strain. Specimen 1 denotes the simulated specimen. Buckling and plastic deformation are both noticeable in some beams of the lattice.

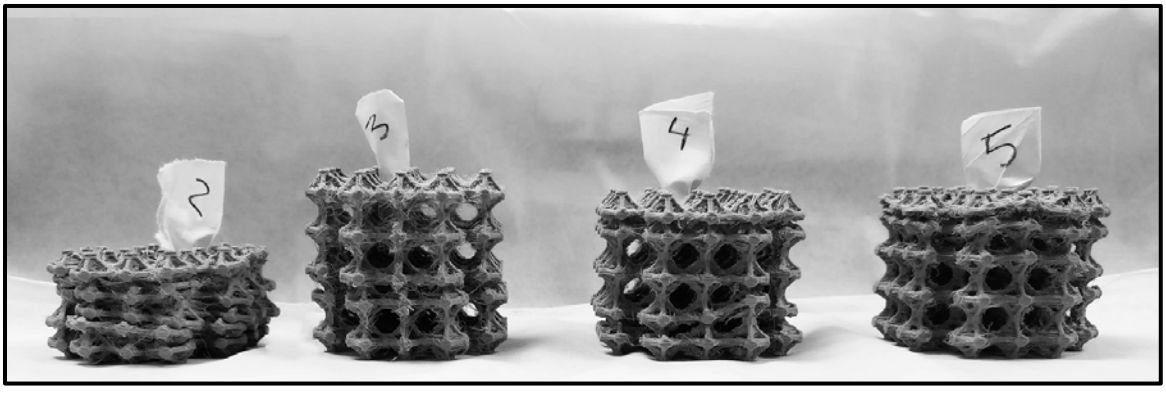

Figure 4.7.2 – 3D Printed Specimens after compressive testing.

Figure 4.7.3 presents a graph of the stress-strain curves acquired from the 3D-printed lattice compression experiments. The peak strain before the first structural failure is shown to be between 5 and 10% strain. Specimens 2, 4, and 5 are shown to return to initial magnitudes of peak stress at strains beyond the first failure point.

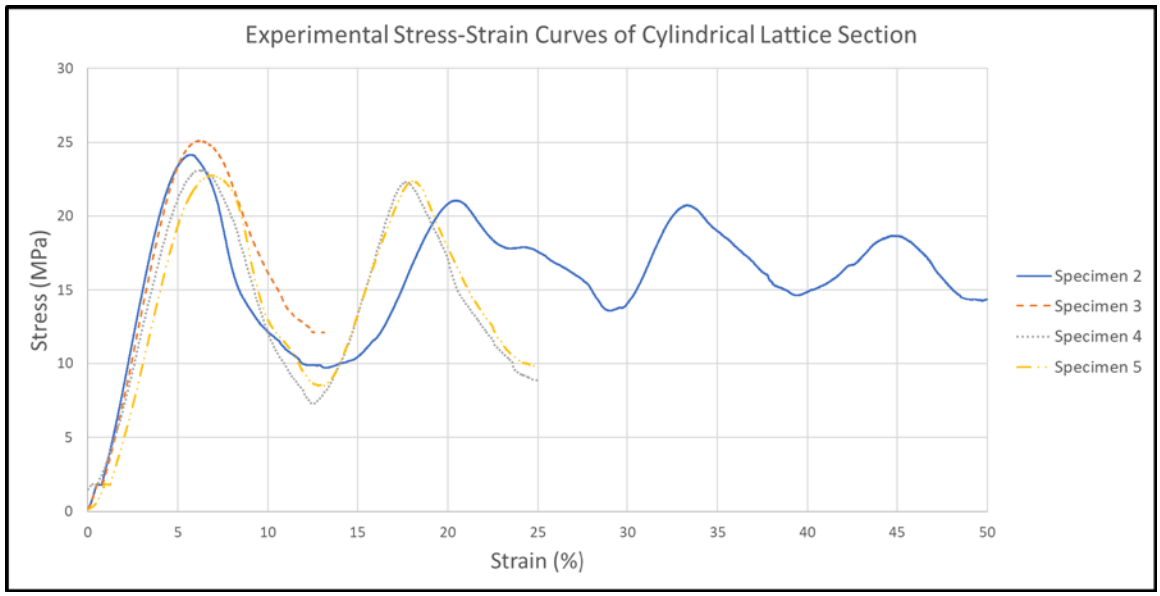

Figure 4.7.3 – Stress-Strain Curves showing the experimental results of mechanically compressing four 3D printed lattice specimens.

Figure 4.7.4 zooms in on the stress-strain curve to help visualize the points used to determine the modulus of each test specimen. Specimens 2 and 3 portray a modulus of 0.62 and 0.61 GPa respectively. Specimens 4 and 5 portray a modulus of 0.53 and 0.52 GPa respectively.

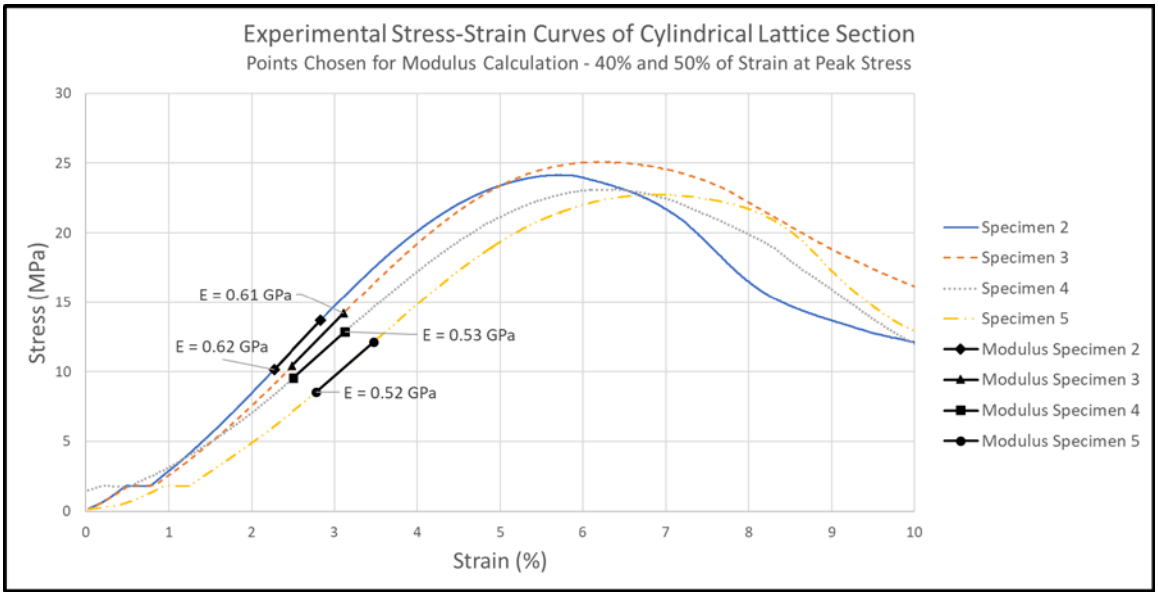

Figure 4.7.4 – Linear elastic region of stress-strain curves with moduli line segments overlaid.

Figure 4.7.5 depicts the linear relationship between the stresses and strains that were found experimentally using a scatter plot. The fit of the linear relationship is described using an R-value of 0.9057.

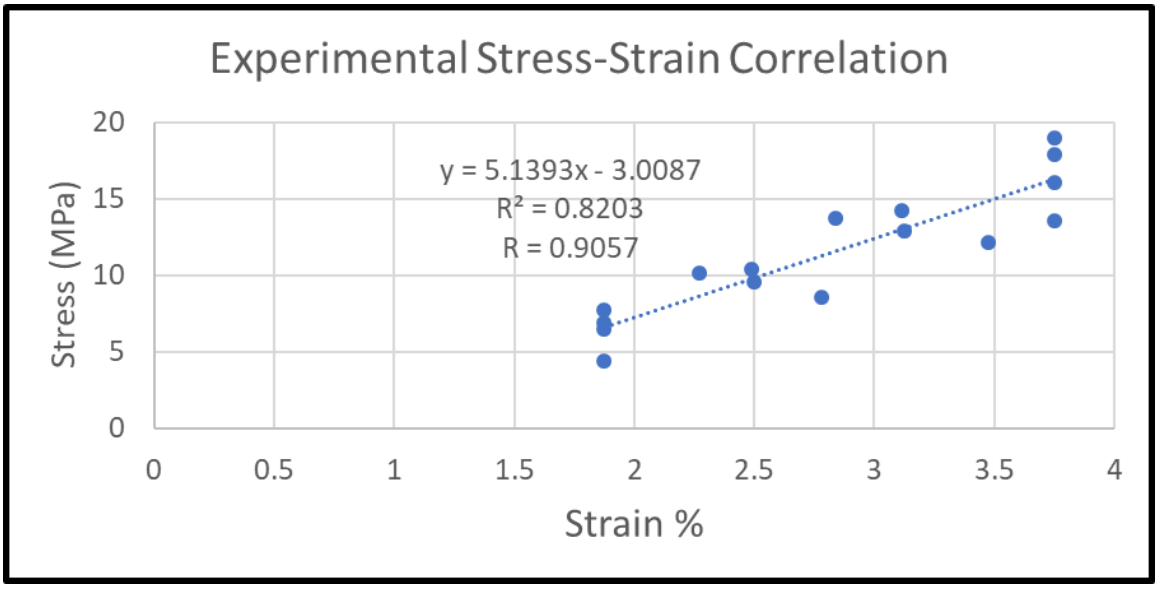

Figure 4.7.5 – Correlation of stress-strain with 4 data points from each sample

4.8 – Simulated Deformation and Stress Distribution of Normal Tibia

Figures 4.8.1, *4.8.2*, and *4.8.3* present the von Mises stress distribution and the axial deformation along the length of the tibia under 1000 N of load for the 2.5 mm thick shell and solid models of the tibia respectively. Note that the visual deformations are unscaled.

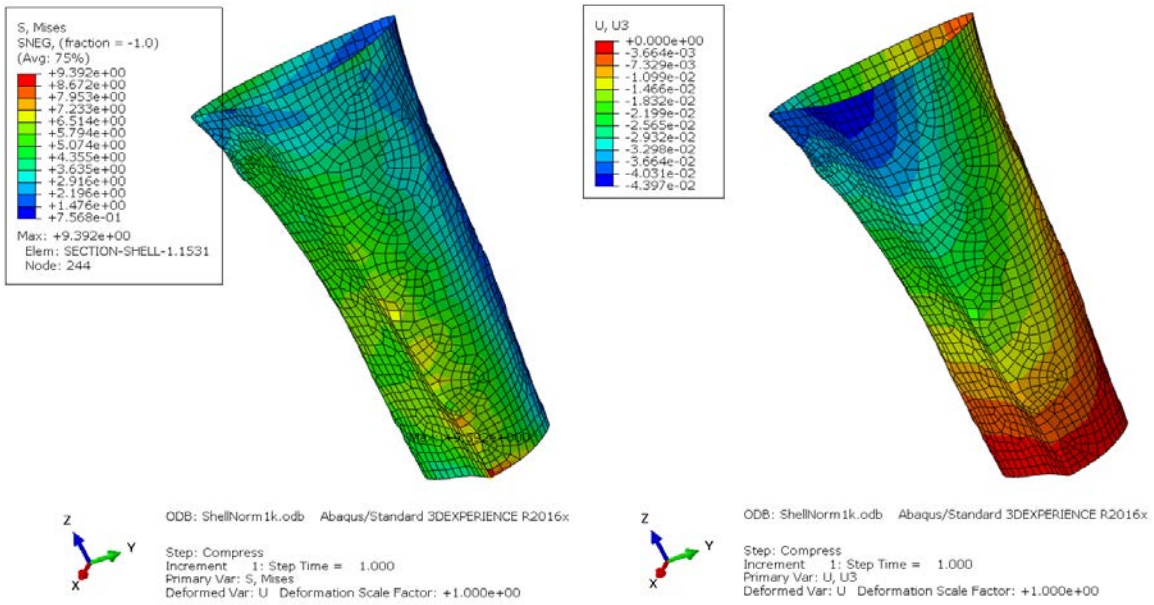

Figure 4.8.1 – 2.5 mm thickness shell under 1000 N load: (Left) Distribution of von Mises stress in MPa, (Right) Axial Deformation in mm

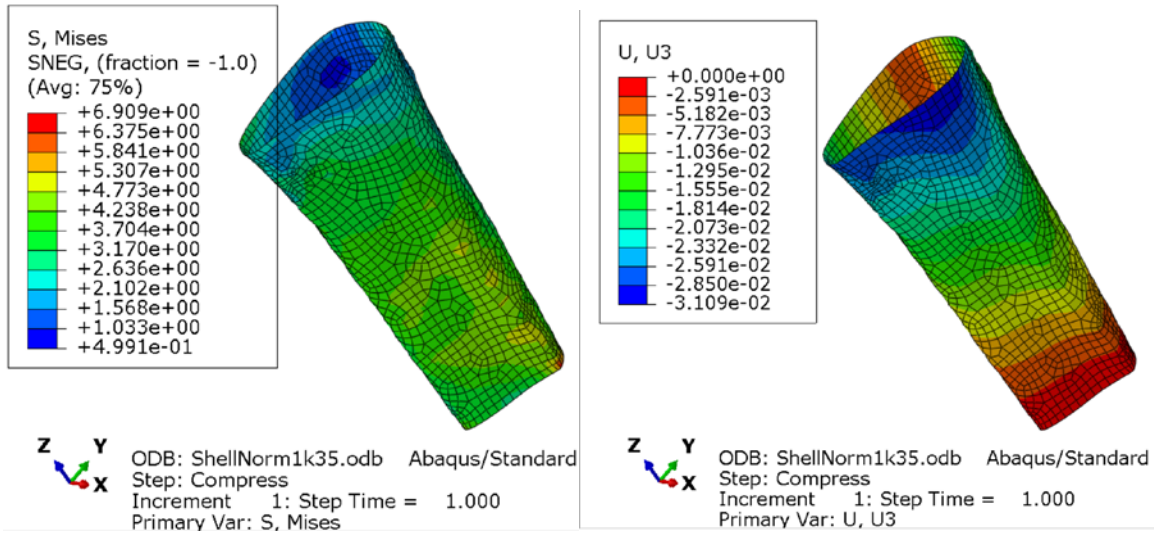

Figure 4.8.2 – 3.5 mm thickness shell under 1000 N load: (Left) Distribution of von Mises stress in MPa, (Right) Axial Deformation in mm

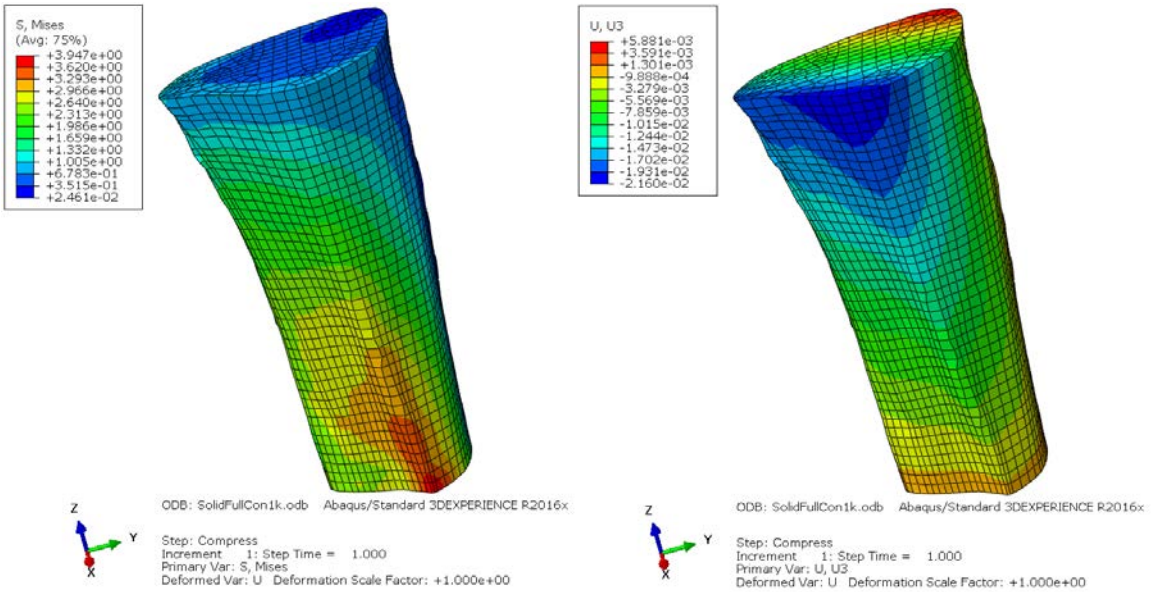

Figure 4.8.2 – Solid tibial section under 1000 N load: (Left) Distribution of von Mises stress in MPa, (Right) Axial Deformation in mm

Tables 4.8.3 and *4.8.4* compares the von Mises stress distribution and the axial deformation found in each compressive loading model with each shell thickness. Note that ABAQUS assumes the model as a linear geometry.

Maximum Stress (MPa) in Normal Tibia Model			
		Compressive Loading Conditions	
		1000 N	2000 N
Shell Thickness	2.5 mm	9.392	18.78
	3.5 mm	6.909	13.82
	Solid	3.947	7.894

Table 4.8.5 – Table showing the resulting maximum Von Mises stresses present in the simulated normal tibia under varying shell thicknesses and compressive loads.

Maximum Axial Deformation (mm) in Normal Tibia Model			
		Compressive Loading Conditions	
		1000 N	2000 N
Shell Thickness	2.5 mm	-0.04397	-0.08795
	3.5 mm	-0.03109	-0.06218
	Solid	-0.0216	-0.0432

Table 4.8.5 – Table showing the resulting maximum axial compressive deformation present in the simulated normal tibia under varying shell thicknesses and compressive loads.

Figure 4.8.5 describes the linear relationship between the stress and strain found in the simulated normal tibia. The simulated modulus, depicted by the slope, ranges from 18.27 GPa for the solid model to 22.23 GPa for the 3.5 mm thick-shelled model. The compressive strain was calculated from the quotient of the maximum axial deformation with the overall axial length of 100 mm.

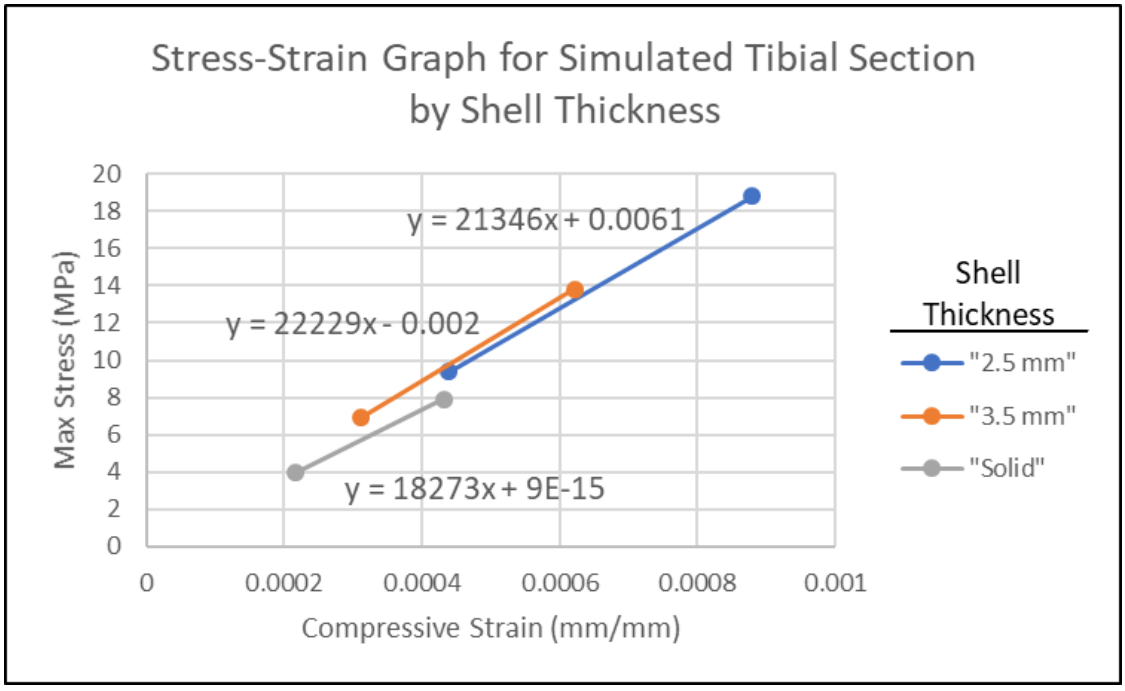

Figure 4.8.6 – Stress strain relationship and associated linear relationship for each shell thickness

4.9 – Simulated Deformation and Stress Distribution of Lattice Implant

Figures 4.9.1 and *4.9.2* present the von Mises stress distribution and the axial deformation along the length of the tibia under 2000 N of load and 1000 N respectively. The von Mises distribution plot was scaled to account for outlier stress values resulting from small elements in the model. The visual deformations of these figures are unscaled. The highest stress regions are shown to occur within the resected bone.

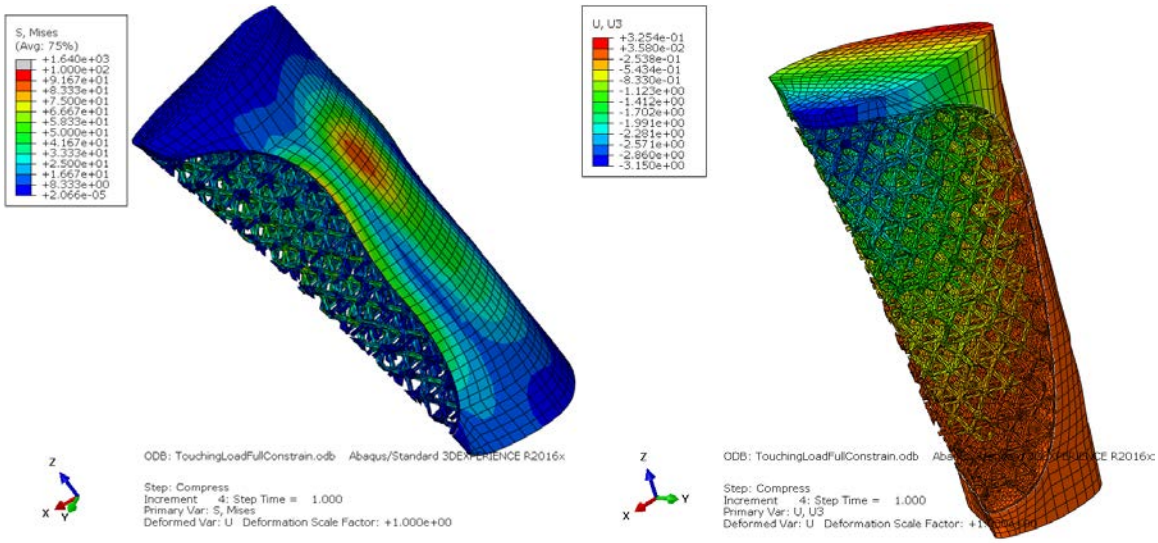

Figure 4.9.1 – Integrated lattice implant under 2000 N load: (Left) Distribution of von Mises stress in MPa, (Right) Axial Deformation in mm

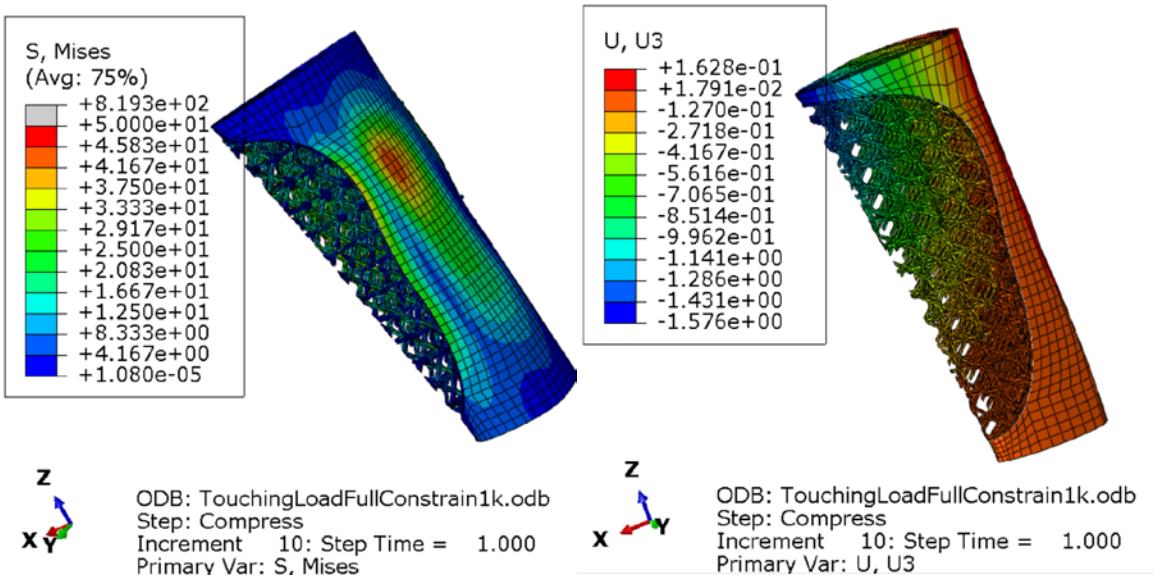

Figure 4.9.2 – Integrated lattice implant under 1000 N load: (Left) Distribution of von Mises stress in MPa, (Right) Axial Deformation in mm

Figure 4.9.3 presents the von Mises stress distribution and the axial deformation along the length of the tibia under 0.5 mm of compressive displacement constrained to the superior surface of the tibial section. The von Mises distribution plot was scaled to account for outlier stress values resulting from small elements in the model. The resected bone was also hidden from the plot to emphasize the distribution across the lattice and its shell. The visual deformations of these figures are unscaled.

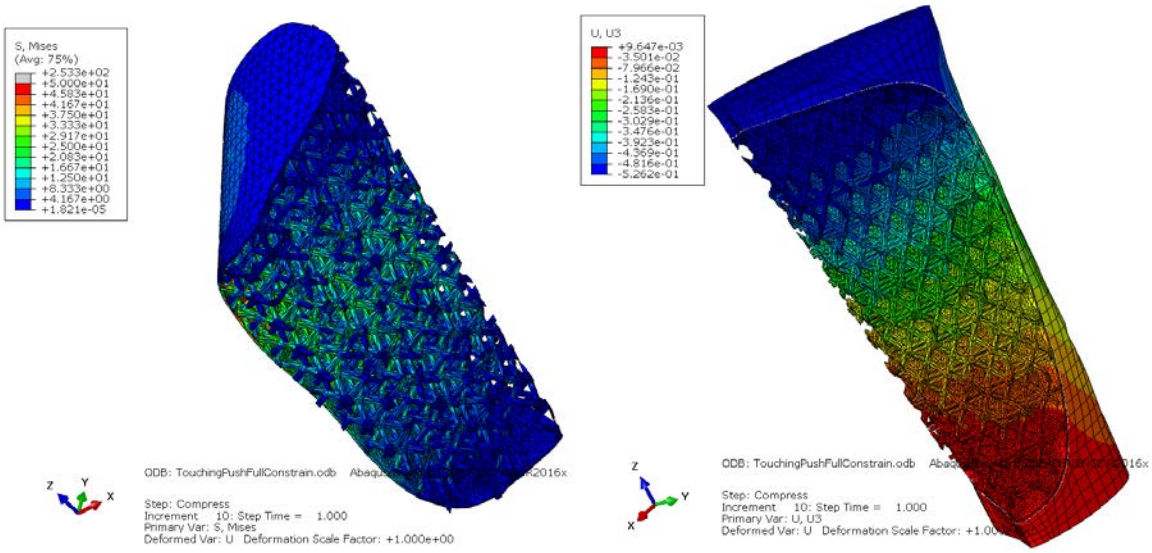

Figure 4.9.3 – Integrated lattice implant under 0.5 mm of compressive displacement: (Left) Distribution of von Mises stress in MPa, (Right) Axial Deformation in mm

Figure 4.9.4 and 4.9.5 displays the stress and strain for the lattice implant at each increment of the compressive load simulations. *Figure 4.9.4* focuses on the 1000 N and 2000 N load models while *Figure 4.9.5* focuses on stress for varying deformations up to 0.5 mm of compressive displacement. The strut with the peak stress typical throughout the lattice was consistently used for each strain value. The peak strut stress ignores the outlying peak stress that may occurs at the locations of small, thin elements unrepresentative of the full lattice behavior. The compressive strain was calculated from the quotient of the maximum compressive axial deformation with the overall axial length of 100 mm.

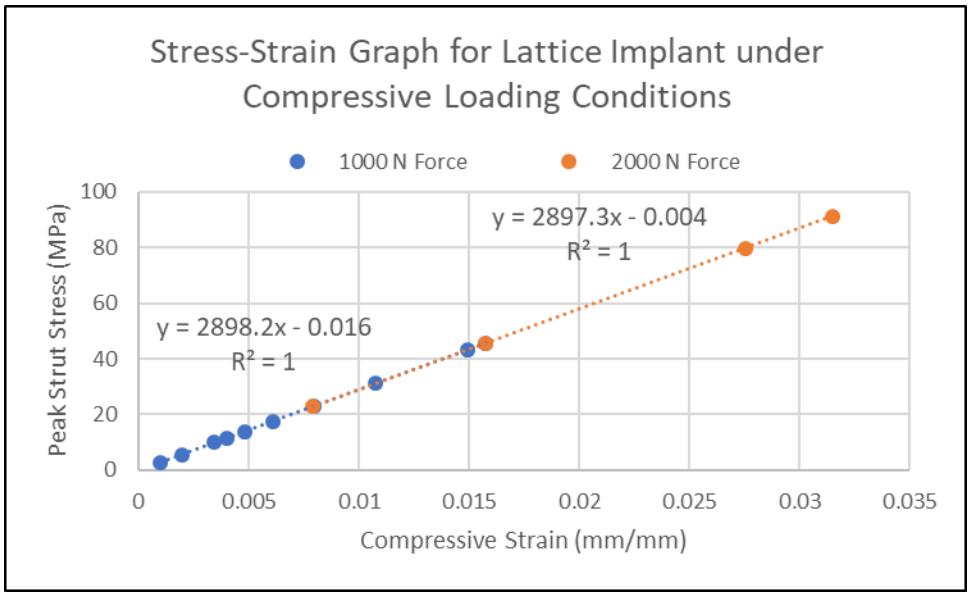

Figure 4.9.4 – Compressive loading stress strain relationship and associated linear relationship for each loading model of the lattice implant

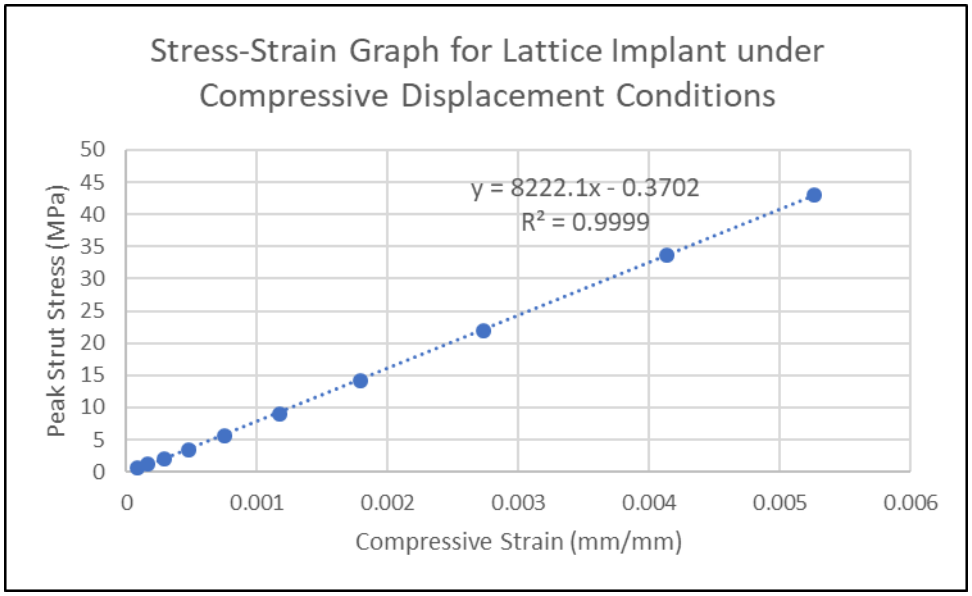

Figure 4.9.5 – Compressive loading stress strain relationship and associated linear relationship for the displacement model of the lattice implant

The typical median stresses present throughout the struts of the lattice implant (depicted in green in Figures 4.9.1 and 4.9.2) were 23.92 MPa for the 1000 N load model, 50.94 for the 2000 N load model, and 26.10 MPa for the 0.5 mm compressive displacement model. This typical value was visually determined based on the peak strut stress and did not entail consistent elements chosen between the models.

Figure 4.9.6 depicts the peak model stress and axial deformation resulting from the 2000 N loading condition on the resected section of the tibia without the lattice implant. The simulation describes a peak stress of 200.1 MPa and a maximum compressive axial deformation of 6.310 mm. The equivalent integrated lattice implant simulation for 2000 N loading conditions reports a peak stress of 91.38 MPa and a maximum compressive axial deformation of 3.150 mm at the same stress location.

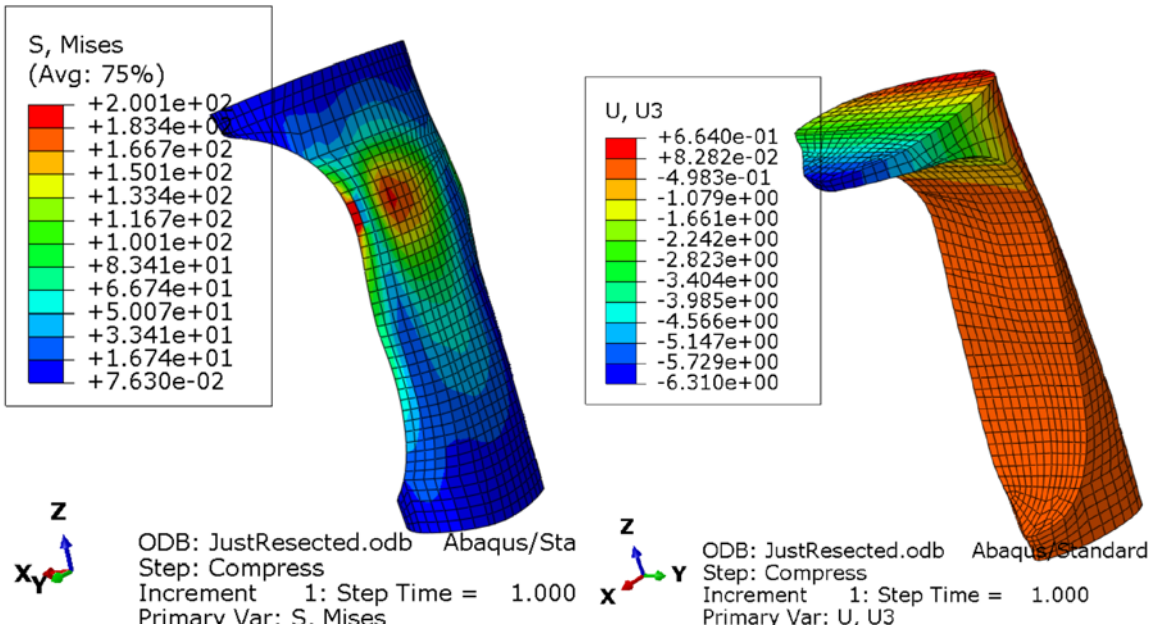

Figure 4.9.6 – Integrated lattice implant under 2000 N of compressive load: (Left) Distribution of von Mises stress in MPa, (Right) Axial Deformation in mm

4.10 – Lattice Implant Integration with 3D Printed Resected Tibia

Figure 4.10.1 and 4.10.2 depict the result of the physical representation of the lattice implant. The physical representation serves as validation for the rapid manufacturing of lattice implant as well as the fit of the implant within the resected tibia. The 3D printed lattice implant used 8.5 g of filament compared to 18 g of filament used for a solid implant within those boundaries. Thus, the lattice reduces mass by 52.78% compared to a solid implant.

Figure 4.10.1 – Physical representation of lattice implant overlaid by the resected tibia

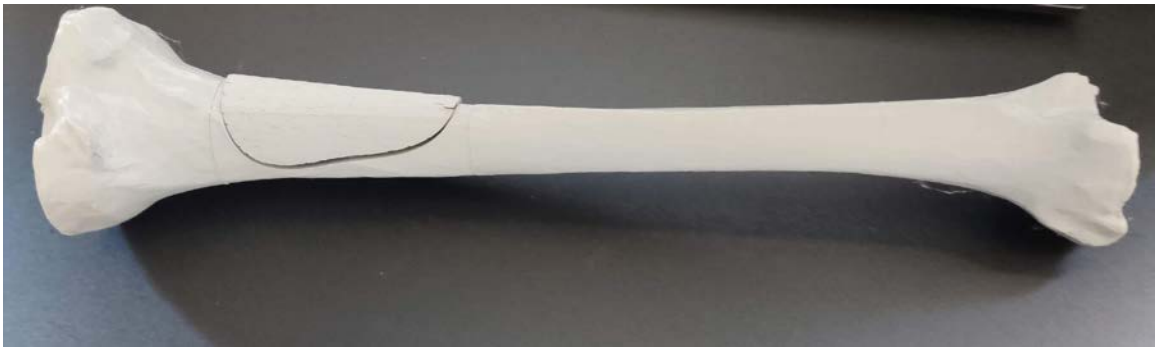

Figure 4.10.2 – Physical representation of lattice implant fit into the resected tibia

Chapter 5: Discussion

5.1 – Assumption of Linearity for Simulated Lattice

First, we consider the impact of voxel pitch on the number of voxels, based on the output information from running the custom program to generate the ABAQUS files. *Figure 4.1.1* depicts the trend for the number of voxels to increase as voxel pitch decreases. The trend fits a power curve with a magnitude of -2.47. As such, the difference in the number of voxels between 3- and 10-mm voxel pitches is more than one order of magnitude greater than the difference in the number of voxels between 10- and 25-mm voxel pitches.

We must consider how the compressive displacement affects the simulation results. Interpretation of the base code from NASA leads us to an assumption of linearity regarding the relationship between the displacement and the resulting peak stress. To use these assumptions, linearity first must be verified with several data points. Using voxel pitches of 7 mm and 10 mm with a beam width of 1 mm, simulations were run at a compressive displacement of 1 mm and at a compressive displacement of 10 mm. *Table 4.1.2* shows how the stress multiplies by 10 for both voxel pitches tested. Crucially, it also shows that this maximum stress is apparent in the exact same beam of the lattice, meaning that the structural performance remains the same, albeit higher stresses.

From the results in *Table 4.1.2*, we determined that a linear relationship exists between stress and displacement, meaning the behavior of the lattice follows the same distribution patterns under higher stresses as the compressive displacement increases. Thus, a comparison between the resulting maximum stress in the lattice and the yield criteria for the material is necessary to determine whether the structure yields. A direct result of this phenomenon is that we can use this assumption of linearity to obtain an

effective elastic modulus for this lattice to compare against the material performance of bone from literature and the performance of PLA as a solid material.

5.2 – Implications of Stress Analysis for Simulated PLA Lattice

With linearity verified, it is safe to continue our simulations with 1 mm of compressive displacement, because the maximum stress at any multiple of 1 mm displacement is the same multiple of maximum stress found at the 1 mm displacement. General trends can readily be seen based on *Table 4.2.1*. A denser lattice (higher number of voxels) leads to a higher maximum von Mises stress that results in the structure. Similarly, a lattice with a thicker beam width generally increases the maximum Von Mises stress that results in the structure. The exceptions to this pattern include the beam width trend present in the highest density lattice when there are over 16000 voxels present. The phenomena of decreasing stress with increasing beam width occurs when the beam width is 1.50 mm or greater. We suggest that the beam width trend is invalidated when the beam width increases beyond one-half the voxel pitch due to beam overlap, but this is inconclusive because this data set is the only instance in our simulations where this holds true. For this combination of parameters, the structural efficiency of the lattice may be overtaken by the solid behavior of the material. Other exceptions to the general trends are increases in peak stress between a 151-voxel lattice (with a pitch of 19 mm) and an 85-voxel lattice (with a pitch of 25 mm). Curiously, the performance of a 234-voxel lattice, with a voxel pitch of 16 mm, exceeds that of the 13 mm pitch lattice and the 19 mm pitch lattice. These two behaviors could result from the methodology used in the lattice generation algorithm. In some cases, extra columns and rows of voxels are attached to the outer boundaries of the generated lattice due to the irregular shape. This results in floating

voxels bounding some regions of the geometry that may contribute to different stress distributions.

Otherwise, the stress quickly increases between beam widths of 0.1 mm and 1 mm, before beginning to converge after 1 mm. Throughout the beam width data sets, the stress tends to make a large dip between a voxel pitch of 8 mm and a voxel size of 9 mm, also representing a dip below the 1000 voxel mark in the structure. It is suggested that the performance benefits of higher density voxels begin at a pitch of 8 mm.

The maximum von Mises stress is typically used as the value to determine whether a structure meets the yield and failure criteria of the material used. By comparing the von Mises stress to yield strength of the PLA material we used, we can determine whether the structure will fail at this maximum stress location. If the structure does not fail, then we can compare the von Mises stress to the ultimate compressive stresses and elastic modulus of bone.

Due to our assumption of linearity outlined in section 1 of chapter 4, we can scale the stresses to estimate overall strain will cause failure. Because PLA is a brittle material and noting that the highest stresses present in *Table 4.2.1* are within 5 MPa of tensile yield strength, this study compares the unscaled simulated data to that of bone. Given a stronger material such as titanium, it would be of interest to scale the stresses to match the strain that causes high damage to trabecular bone. A study by Notre Dame researchers suggests a range of 2.50% to 4.50% compressive strain for highly damaged trabecular framework (Garrison, Gargac, and Niebur, 2011). The average effective strain from our model was 0.27%. Scaling it by 10 would put the structure with this range and depict von Mises stresses as high as 340 MPa, but the limitations of PLcamA would cause the structure to

break first. The Notre Dame paper cites an elastic modulus of trabecular bone of 2.3 GPa found with those applied strains, whereas the highest performing voxel lattices simulated have an elastic modulus of over five times that amount after being simulated with PLA.

5.3 – Determining Effective Structural Length of Simulated Lattice

To better compare our results to bone performance reported in the literature and the performance of various materials on the Ashby chart, it is of use to calculate an effective elastic modulus based on the results of the study. Due to the verification of linearity, we can safely assume, given a stress Y at strain X, that the stress will be 10 Y at strain 10 X. Thus, a simplified elastic modulus calculation would be $E = \frac{10\,Y - Y}{10\,X - X} = \frac{9\,Y}{9\,X} = \frac{Y}{X}$ such that the modulus would be *Y* divided by *X*. With our displacement of 1 mm, our strain *X* is equal to 1 mm divided by the effective structural length along the axis of displacement. Thus, our structure has an effective strain of 1 mm divided by an effective structural length *L*. In our modulus calculation, this reduces to modulus $E = LY$.

The total structural length varies based on the voxel pitch because only so many whole units of voxels can evenly divide the imported scan along the axis of displacement. In the program, all vertices that have a value greater than 365 mm on the displacement axis fully fixed. Thus, we could assume that 365 mm is our effective structural length, the length that is compressible. However, this is not accurate because the first set of fixed vertices may be located greater than 365 mm on the displacement axis. To account for this, we can use our understanding of voxel geometry to calculate an effective structural length representing the compressible distance between the first fixed set of vertices in the structure and the displaced end of the structure. We recognize that the program begins generating sets of voxel center points starting at the one end of the scanned specimen, never surpassing

the length of the scanned specimen. The length of the resulting structure is determined by the maximum number of center points that can fit within the length of the scanned specimen. In addition, a half voxel length is added to either end of the structure. Thus, the total length of the structure increases by one whole voxel length. Vertices exist at every half-voxel length because a voxel is separated into upper and lower halves of an octagon by a set of middle vertices. The position of first vertices on the displacement axis beyond 365 mm can be calculated by dividing the remainder of the difference, between the total length and 365 mm, by the half-voxel length and adding it to 365 mm. Simply put, the calculation is

$$L = 365\ mm + [(TotalLength - 365\ mm)\ modulo\ HalfVoxelLength].$$

The results of this calculation can be seen in *Table 4.3.1* for the given voxel pitches. The lengths were verified using the query tool in the ABAQUS CAE visualization interface.

5.4 – Effective Modulus of the Simulated PLA Lattice

Having determined the effective structural length *L* for the given voxel pitches, we understand that the effective structural strain is $\varepsilon = 1mm / L$. Thus, the effective elastic modulus is calculated with $E = Y/\varepsilon$. We divided our modulus by 1000 to get a value in GPa for easier comparison to literature. The results of the calculation are shown in *Table 4.4.1* and visualized in *Figure 4.4.2*.

The elastic modulus is often noted as the slope of the stress-strain curve or as a resistance to elastic deformation. Because this quantity is not dependent on the individual strain, it is a good value to use for a comparison of material performance. The calculation of modulus was reduced to stress scaled by the effective structural strain, which varied slightly between voxel pitches because the change in length was constant. While we could

have used a constant of 370 mm to estimate the effective structural length, it was important to have an accurate representation of effective strain for future comparisons. As such, we found the average effective structural length to be 370.7 mm with a standard deviation of about 3.5 mm, resulting in an effective strain of 0.270 % ± 0.0026 %.

The effective elastic modulus ranges from 2.5 to 12.5 GPa depending on beam width and voxel density. The same trends that applied for maximum stress also hold for elastic modulus, such that a higher voxel density lattice with a larger beam width results in a higher effective elastic modulus. For potential bone repair applications discussed in this work, the design goal would be to maximize the hollow space of the object. This minimizes voxel density, to improve the feasibility of manufacturing, to improve the structure's strength to weight performance, and to produce enough room for the bioactive ions and seeded bone-forming cells to exist. The stress analyses reported in section 5.1 and *Figure 4.4.3* are used to suggest a voxel pitch of 8 mm (1245 total voxels) be used for making a scaffold. An 8 mm voxel pitch is suggested because the elastic modulus begins to converge after that number of total voxels for all tested beam widths. Additionally, a beam width of 2.00 mm is suggested for making a scaffold, because there exists a greater surface area for any seeded cells or ions to adhere to, increasing the functionality of the lattice beyond its strength to weight performance.

In section 2 of chapter 2, the experimental and averaged values of cancellous bone were discussed. Gibson and Ashby (1997) report the elastic modulus of trabeculae to be 12 GPa. Trabeculae in the human tibia are reported to have an elastic 14.8±1.4 GPa based on a Harvard study (Oftadeh et al., 2015). At a voxel pitch of 8 mm and a beam width of 2 mm, the elastic modulus of the lattice is 11.60 GPa. This means the performance of the

lattice constructed from PLA with these parameters is 97% of performance cited by Gibson and Ashby and is 78% of performance cited by the Harvard study. It is important to note, however, that tested lattice is constructed from the brittle PLA material tested with the material's average elastic modulus. Given a stronger plastic polymer or even a titanium alloy, the modulus is assumed to increase. However, ease of manufacturing may decrease, and manufacturing cost may increase with these higher performing materials. Early studies have shown the viability of titanium metal 3D printing for both bone implants (Popov et al., 2018). Additional studies have demonstrated titanium 3D printing for trabecular bone reconstruction (Y. Zhang et al., 2018). The performance of the simulated PLA lattice at voxel pitches below 4mm surpasses the performance cited by Gibson and Ashby for trabecular bone. This study concludes that the engineered lattice can rival the performance of trabecular bone.

5.5 – Simulated Lattice Performance with Other Materials

Tables 4.5.1 and 4.6.1 as well as *Figures 4.5.2*, *4.5.3*, *4.6.2*, and *4.6.3* focus on the performance of the simulated lattice when other materials, Titanium alloy Ti-6Al-4V and thermoplastic Ultem 2200, are applied. The titanium alloy was considered due to its use in orthopedic implants and to demonstrate the performance differences that a metallic construction provides compared to plastic. The thermoplastic Ultem 2200 was considered due to its demonstrated success with the lattice when injection molded for aerospace applications. The application of the thermoplastic is shown to demonstrate the performance variations between different plastic materials.

The metallic construction of the lattice with the titanium alloy implies its use as a more permanent scaffold rather than a biodegradable scaffold meant for bone regeneration.

However, the titanium lattice could still serve as a cellular scaffold as demonstrated by recent studies (Y. Zhang et al., 2018). For a lattice of pitch 8mm and beam width 2mm, the titanium alloy provides a 4086% increase over the modulus simulated for PLA. Similarly, the Ultem 2200 thermoplastic provides a 241% increase over the modulus simulated for PLA. The highest simulated modulus is 12.5 GPa with PLA, 510.2 GPa with titanium, and 30.2 GPa with Ultem 2200. The performance increases that result from material choices suggest that further study into the optimal material would be of interest to optimize lattice performance.

A consistent behavioral pattern in *Figures 4.2.2*, *4.5.2*, and *4.6.2* is found. This pattern, emphasized in *Figure 4.6.4*, suggests that the relative structural performance of the lattice is independent of the material when compared with lattices of the same material. Thus, the performance of the lattice simply scales as an effect of the material. Because the simulation focuses on the material properties of elastic modulus, density, and Poisson's ratio, the scaling factor is the ratio of the elastic moduli of the materials.

5.6 – Experimental Validation of Computational Model

It was assumed that the stress in the mechanically compressed lattice structure was the highest stress present in any beam of the structures. The stress found through simulation was the maximum stress present in any single beam. Stress is based on surface area, so we determined the effective surface area of the structure to be the solid volume (calculated during model generation) divided by the structure's height. The mass of the simulated lattice is based on a simplified model and an assumed density of 1.25 g/cm^3 for PLA. Modulus was calculated based on the slope formula between points of stress located at 40%

and 50% of the strain at peak stress to be consistent regardless of variations of the zero position. These points and the resulting moduli are visualized in *Figure 4.7.4*.

Catastrophic failure in the beams was expected due to prior lattice compression research, but catastrophic failure did not occur in the experiment. This suggests that fracture patterns are partially dependent on the lattice's material. Based on *Figure 4.7.3*, the experimental results were shown to follow a consistent pattern of failure. From observation, the first failure is reached when the first strut collapsed. The horizontal plane of voxels that contained the failed strut quickly followed in failure. Although one plane collapsed, the structure can withstand similar compressive loads before another failure occurs. The extended results of specimen 2 beyond 25% strain suggest that this pattern continues with each horizontal plane, but this suggestion requires further trials to 50% strain to be conclusive.

The experimental results shown in *Table 4.7.1* depict that stresses and moduli are consistently below expectations from the simulations with the same points of strain used. It is evident that specimens 2 and 3 had similar performance as did specimens 4 and 5. The mass of specimens 3 and 4 were less than specimens 2 and 3. It is suggested that inconsistencies with the post-processing of the print likely contributed to the mass differential and the slight differences in structural integrity. Because the experimental moduli are 28.16% of the simulated effective modulus with a standard deviation of 2.33%, it is suggested that there is consistent behavior for printed specimens compared to their simulated counterparts. The simulation is idealized and assumes a perfect continuum material of PLA and does not account for delamination between the thin 3D printed layers. The behavior of the lattice may differ when printed in a different orientation, which

requires further testing. The experimental results suggest that, at least for a lattice constructed from PLA, the experimental modulus of mechanically compressing a 3D printed lattice of the tibial bone section will be 28.16% ± 2.33% of the simulated modulus. The qualitative results shown in *Figure 4.7.2* depict plastic deformation because of the high strain. Furthermore, specimen 2 measures 23 mm in height although it was a 40 mm structure compressed 20 mm, suggesting some elastic recovery. The deformation behavior of the experimental lattice is preferable to catastrophic failure due to the potential bone repair applications previously discussed.

Figure 4.7.5 uses a scatter plot to correlate the relationship between stress and strain from 4 data points from each of the tested lattices. The scatter plot depicts a linear trend with an R-value of 0.9057, confirming that the assumption of linearity described in section 5.1 can be demonstrated experimentally.

5.7 – Structural Behavior of Normal Tibial Model

The design of an implant based on the lattice structure for the replacement of a tumorous bone region assumed the favorable properties demonstrated by the simulated bone facsimiles and the printed cylindrical lattices. The lattice implant design was implemented for a nonuniform boundary of a small portion of a long bone. Thus, an analysis of the stress distribution and the axial deformation of a section of an unafflicted tibia was necessary as a point of comparison to the performance of lattice implant.

The stress and displacement were found to precisely scale by the compressive loading conditions among every instance of the simulated tibia model such that the 2000 N load exhibited twice the axial displacement and maximum stress than that of the 1000 N load. The simulation is idealized such that ABAQUS assumes the model to be a linear

geometry which suggests a proportional relationship between load and displacement. *Tables 4.8.3* and *4.8.4* depict a 26.4% decrease in maximum stress and a 29.9% decrease in axial displacement between the 2.5 mm shell and the 3.5 mm shell. There is a 42.87% decrease in maximum stress and a 30.52% decrease in axial deformation between the 3.5 mm shell and the solid model. For the 2000 N model, the maximum axial deformation by any of the models was 0.088 mm. Assuming proportional scaling of load and displacement, a lattice implant model simulating compressive displacement of 0.5 mm would be reasonably sufficient for loads up to 11000 N. The axial modulus of the normal tibia under the simulated loading conditions averaged to be 20.61 GPa ± 1.70 GPa, which is greater than the material elastic modulus of 14.8 GPa set for this geometry. The greater modulus may result from the use of the axial strain in the modulus calculation whereas the load was coupled across the superior surface and edges of the irregular geometry of tibial model. The tibial geometry is noted to have slight deformations along other axes which can affect the modulus calculation. Both the two shell models and solid model produced similar distributions of stress and deformation which are shown visually in *Figures 4.8.1*, *4.8.2*, and *4.8.3* suggesting that the exterior geometry is the primary factor in the distribution.

5.8 – Structural Behavior of Integrated Lattice Implant

The critical analysis of this model is to understand the interaction between the lattice implant and the resected tibia. Previous sections of this chapter discussed the behavior of the isolated lattice structure in irregular geometry. Specifically, the implant is shown to distribute stress from the resected bone across the lattice. As expected from the linear relationship of the load and deformation from the simulation of the normal tibia section, the stress distribution of the model under 1000 N and 2000 N of load is similar as

per *Figures 4.9.1* and *4.9.*2. The individual stresses from these models are scaled based on the load. From *Figure 4.9.3*, the linear relationship of the incremental stresses and strains taken to achieve the desired compressive loading conditions can be seen with an R^2 of 1. The stress strain relationship for the 1000 N loading condition overlaps with the early strains taken to achieve the 2000 N loading condition. The resulting axial modulus of the lattice implant is 2.90 GPa under these loading conditions. This modulus is greater than the underlying material modulus of PLA of 2.79 GPa.

Unlike the compressive loading conditions, the simulation of compressive displacement compressed the entire superior surface of the integrated lattice model by the allotted 0.5 mm. The simulations of compressive loading depicted that the medial aspect of the surface will deform in tension while the lateral region with the underlying lattice will deform in compression. This behavior is consistent with the loading simulations of the normal tibia in *Chapter 5.8*. Thus, it is evident from *Figure 4.9.3* that the stress distribution and deformation behavior differ from the loaded simulations. The model evenly deforms as the model is squished. The stress distribution is thus focused on the voxels connected to the thinnest part of the bone where the resection made the deepest incision. In *Figure 4.9.5*, the linear relationship between the strains and stresses of the compressive displacement model is depicted with an R^2 of 0.9999. The resulting axial modulus of the lattice implant is 8.22 GPa under compressive displacement as opposed to the 2.90 GPa modulus found with the compressive load. This phenomenon may result from some tensile forces acting on the voxels due to the medial aspect of the bone deforming in tension from the compressive load.

From *Figure 4.9.*6, a comparison can be made between the integrated lattice implant and the resected tibial section without implant. The maximum stress on the bone decreased from 200.1 MPa to 93.38 MPa giving a 54.33% decrease. Maximum axial deformation is also shown to decrease from 6.310 mm to 3.150 mm resulting in a decrease of 50.07%.

5.9 – Feasibility of Manufacturing Methodology of Lattice Implant

The physical model of the lattice implant manufactured via traditional FDM printed was completed in 6 hours at high resolution without support structure. It is estimated that the lattice can be printed in under 4 hours with a slightly lower resolution and faster print speeds without loss of quality. The outer shell of the lattice had minor fracture issues when removing from the print bed due to the shell only being 0.254 mm thick. Future models would be improved with an increase of the outer shell thickness to 0.4 mm, which is the nozzle diameter of the printer. As per *Figure 3.9.1,* Small print artifacts shaped like strings are apparent between the struts of the lattice due to the lack of interior support material for the lattice that complicates post processing. A lattice implant printed with water soluble support preventing the strings but required 24 hours of post processing in a circulating water bath. It is suggested that future models be printed using stereolithography (SLA) printers that provide micron accuracy without the need for support. However, SLA printers require some post-processing in the form of ultraviolet treatment. In addition, the performance of the underlying resin material with the lattice implant is unknown as opposed to PLA. The fit of the lattice implant within the printed tibial specimen is shown in *Figures 4.10.1* and *4.10.2*. The lattice contours to the ideal model of the unafflicted tibia; however, the printed implant requires slight tolerance modifications to fit perfectly.

5.10 – Future Applications

The application of this lattice is not limited to bone grafts and prosthetics; an intramedullary nail constructed from this lattice with a biocompatible material could provide the benefits of this technology to long bone fracture treatments. This lattice structure would ultimately be constructed out of biocompatible materials to aid in natural bone regeneration processes and be seeded with osteogenic gels to create new bone.

This study employed a manual method of generating a lattice within the boundaries of the implantable structure that requires extensive training in use of the modeling software and significant computational resources to process the geometry. Initial investigations were undertaken into the implementation of this manual method as an automated model given a resected tibial geometry. This automated process would ideally extract the afflicted tibial geometry from a CT scan and subtract the cancerous regions to recommend an incision curve for tumor removal. Based on this curve, the program would estimate the boundaries of a potential implant and consequently generate a lattice structure and outer shell. The program would return a geometric model highlighting the tumor and its recommended region of resection as well as a 3D printable file of the lattice implant.

5.11 – Conclusions

In this study, we have produced and simulated a lattice that can resemble natural bone performance. A bone facsimile was generated with an octahedron lattice internal structure based on a 3D scan of a cadaveric tibia. This bone facsimile has been tested using finite element analysis to suggest an optimal voxel density and beam width at which the internal structure has a high elastic modulus to relative density ratio for use as a scaffold during bone reconstruction. Comparative simulations of the lattice’s performance with

different materials have been shown. Lattice specimens were 3D printed and mechanically compressed to verify assumptions present in the simulation, resulting in a behavioral pattern for printed lattices compared to simulated lattices. A lattice implant was designed for the replacement of an osteosarcoma-afflicted tibia. The lattice implant was simulated to validate its structural viability under typical bodyweight loading conditions. The implant was 3D printed to verify its feasibility of manufacturing.

Strong but lightweight artificial structures can help patients regain comparable functions that natural bone provides due to its strength and density. Future work on this topic would include a concrete placement on the Ashby chart comparing the strength to weight of a material as well as the effect of a cortical boundary on the lattice. Additional mechanical testing should be done to determine the effect of print orientation on lattice performance. Further investigations into automation of lattice implant generation should be considered. Alternative 3D biocompatible printing materials to PLA should be tested for the manufacturing of the lattice implant. The authors of this study hope to pave the way for the next generation of bone implants or scaffolds based on the favorable structural properties of voxel lattices.

References

"3D-Printable Prosthetics | e-NABLE." 2019. https://3dprint.nih.gov/collections/prosthetics.

"Overview of Materials for Polylactic Acid (PLA) Biopolymer." 2019. MatWeb. 2019. http://www.matweb.com/search/DataSheet.aspx?MatGUID=ab96a4c0655c4018a8785ac4031b9278.

"PLA and ABS Strength Data." 2014. MakerBot. May 14, 2014. https://downloads.makerbot.com/legal/MakerBot_R__PLA_and_ABS_Strength_Data.pdf.

Amin, S., S. J. Achenbach, E. J. Atkinson, S. Khosla, and L. J. Melton. 2014. "Trends in Fracture Incidence: A Population-Based Study Over 20 Years." *Journal of Bone and Mineral Research : The Official Journal of the American Society for Bone and Mineral Research* 29 (3): 581–89. https://doi.org/10.1002/jbmr.2072.

Arun, K. V., and K. K. Jadhav. 2016. "Behaviour of Human Femur Bone Under Bending and Impact Loads." *European Journal of Clinical and Biomedical Sciences* 2 (2): 6. https://doi.org/10.11648/j.ejcbs.20160202.11.

Cheung, Kenneth C. 2012. "Digital Cellular Solids : Reconfigurable Composite Materials." MIT. http://oatd.org/oatd/record?record=handle%5C%3A1721.1%5C%2F78199.

Cheung, Kenneth C., and Neil Gershenfeld. 2013. "Reversibly Assembled Cellular Composite Materials." *Science* 341 (6151): 1219–21. https://doi.org/10.1126/science.1240889.

Cheung, Kenneth C., Daniel Cellucci, Grace Copplestone, Nick Cramer, Jesse Fusco, Ben Jenett, Joseph Kim, et al., 2017. "Development of Mission Adaptive Digital Composite Aerostructure Technologies (MADCAT)." In. https://doi.org/10.2514/6.2017-4273.

Cramer, Nicholas B., Daniel W. Cellucci, Olivia B. Formoso, Christine E. Gregg, Benjamin E. Jenett, Joseph H. Kim, Martynas Lendraitis, et al., 2019. "Elastic Shape Morphing of Ultralight Structures by Programmable Assembly." *Smart Materials and Structures* 28 (5): 055006. https://doi.org/10.1088/1361-665X/ab0ea2.

de Azevedo, J. W., Fernandes, T. A., Fernandes, J. V., de Azevedo, J. C., Lanza, D. C., Bezerra, C. M., Andrade, V. S., de Araújo, J. M., Fernandes, J. V."Biology and pathogenesis of human osteosarcoma (Review)". Oncology Letters 19.2 (2020): 1099-1116.

DeBoer, J., M. A. Witlox, G. J. L. Kaspers, and B. J. van Royen. 2011. “Molecular Alterations as Target for Therapy in Metastatic Osteosarcoma: A Review of Literature.” Clinical & Experimental Metastasis 28 (5): 493–503. https://doi.org/10.1007/s10585-011-9384-x.

Ene R, Sinescu RD, Ene P, et al. Proximal tibial osteosarcoma in young patients: early diagnosis, modular reconstruction. Romanian Journal of Morphology and Embryology = Revue Roumaine de Morphologie et Embryologie. 2015 ;56(2):413-417.

Farah, Shady, Daniel G. Anderson, and Robert Langer. 2016. “Physical and Mechanical Properties of PLA, and Their Functions in Widespread Applications - A Comprehensive Review.” *Advanced Drug Delivery Reviews* 107: 367–92. https://doi.org/10.1016/j.addr.2016.06.012.

Fryar, Cheryl D., Deanna Kruszon-Moran, Qiuping Gu, and Cynthia L. Ogden. 2018. “Mean Body Weight, Height, Waist Circumference, and Body Mass Index Among Adults: United States, 1999-2000 Through 2015-2016.” National Health Statistics Reports, no. 122: 1–16.

Garrison, Jacqueline G., Joshua A. Gargac, and Glen L. Niebur. 2011. “Shear Strength and Toughness of Trabecular Bone Are More Sensitive to Density than Damage.” *Journal of Biomechanics* 44 (16): 2747–54. https://doi.org/10.1016/j.jbiomech.2011.09.002.

Gibson, Lorna J., and Michael F. Ashby. 1997. *Cellular Solids: Structure and Properties*. 2nd ed. Cambridge Solid State Science Series. Cambridge University Press. https://doi.org/10.1017/CBO9781139878326.

Gregg, Christine E., Joseph H. Kim, and Kenneth C. Cheung. 2018. “Ultra-Light and Scalable Composite Lattice Materials.” *Advanced Engineering Materials* 20 (9): 1800213. https://doi.org/10.1002/adem.201800213.

Gregor, Aleš, Eva Filová, Martin Novák, Jakub Kronek, Hynek Chlup, Matěj Buzgo, Veronika Blahnová, et al., 2017. “Designing of PLA Scaffolds for Bone Tissue Replacement Fabricated by Ordinary Commercial 3D Printer.” *Journal of Biological Engineering* 11 (October). https://doi.org/10.1186/s13036-017-0074-3.

Hahn, M., M. Vogel, M. Pompesius-Kempa, and G. Delling. 1992. “Trabecular Bone Pattern Factor—a New Parameter for Simple Quantification of Bone Microarchitecture.” *Bone* 13 (4): 327–30. https://doi.org/10.1016/8756-3282(92)90078-B.

Huang, Junqi & Bi, Wenzhi & Han, Gang & Jia, Jinpeng & Xu, Meng & Wang, Wei. (2018). The multidisciplinary treatment of osteosarcoma of the proximal tibia: A retrospective study. BMC Musculoskeletal Disorders. 19. 315. 10.1186/s12891-018-2245-x.

Jenett, Benjamin, Daniel Cellucci, Christine Gregg, and Kenneth C. Cheung. 2016. "Meso-Scale Digital Materials: Modular, Reconfigurable, Lattice-Based Structures." In, V002T01A018. https://doi.org/10.1115/MSEC2016-8767.

Jenett, Benjamin, Sam Calisch, Daniel Cellucci, Nick Cramer, Neil A Gershenfeld, Sean Swei, and Kenneth C. Cheung. 2016. "Digital Morphing Wing: Active Wing Shaping Concept Using Composite Lattice-Based Cellular Structures." *Soft Robotics* 4 (October). https://doi.org/10.1089/soro.2016.0032.

Kenkre, J. S., and Jhd Bassett. 2018. "The Bone Remodelling Cycle." Annals of Clinical Biochemistry 55 (3): 308–27. https://doi.org/10.1177/0004563218759371.

Klein, Michael & Siegal, Gene. (2006). Osteosarcoma Anatomic and Histologic Variants. American journal of clinical pathology. 125. 555-81. 10.1309/UC6K-QHLD-9LV2-KENN.

Lantada, Andrés Díaz, and Pilar Lafont Morgado. 2012. "Rapid Prototyping for Biomedical Engineering: Current Capabilities and Challenges." *Annual Review of Biomedical Engineering* 14 (1): 73–96. https://doi.org/10.1146/annurev-bioeng-071811-150112.

Li, B., and R. M. Aspden. 1997. "Composition and Mechanical Properties of Cancellous Bone from the Femoral Head of Patients with Osteoporosis or Osteoarthritis." Journal of Bone and Mineral Research: The Official Journal of the American Society for Bone and Mineral Research 12 (4): 641–51. https://doi.org/10.1359/jbmr.1997.12.4.641.

Lindsey, Brock A., Justin E. Markel, and Eugenie S. Kleinerman. 2016. "Osteosarcoma Overview." Rheumatology and Therapy 4 (1): 25–43. https://doi.org/10.1007/s40744-016-0050-2.

Majuta, Lisa A., Geraldine Longo, Michelle N. Fealk, Gwen McCaffrey, and Patrick W. Mantyh. 2015. "Orthopedic Surgery and Bone Fracture Pain Are Both Significantly Attenuated by Sustained Blockade of Nerve Growth Factor." *Pain* 156 (1): 157–65. https://doi.org/10.1016/j.pain.0000000000000017.

McCarthy, Edward F., and Frank J. Frassica. 2014. "Primary Bone Tumors." In *Pathology of Bone and Joint Disorders: With Clinical and Radiographic Correlation*, 2nd ed., 187–272. Cambridge University Press. https://doi.org/10.1017/CBO9781139946247.013

Meyers, M.A., and P.Y. Chen. 2014. *Biological Materials Science: Biological Materials, Bioinspired Materials, and Biomaterials*. Cambridge University Press. https://books.google.com/books?id=Ufs6BAAAQBAJ.

Nisbett, Keith, and Richard G. Budynas. 2015. *Shigley's Mechanical Engineering Design, 10th Edition*.

Nyman, Jeffry S., Anuradha Roy, Xinmei Shen, Rae L. Acuna, Jerrod H. Tyler, and Xiaodu Wang. 2006. “The Influence of Water Removal on the Strength and Toughness of Cortical Bone.” Journal of Biomechanics 39 (5): 931–38. https://doi.org/10.1016/j.jbiomech.2005.01.012.

Oftadeh, Ramin, Miguel Perez-Viloria, Juan C. Villa-Camacho, Ashkan Vaziri, and Ara Nazarian. 2015. “Biomechanics and Mechanobiology of Trabecular Bone: A Review.” *Journal of Biomechanical Engineering* 137 (1): 0108021–215. https://doi.org/10.1115/1.4029176.

Ottaviani, Giulia & Jaffe, N.. (2010). The epidemiology of osteosarcoma. 10.1007/978-1-4419-0284-9.

Patterson, Jason, Chamnanni Rungprai, Taylor Den Hartog, Yubo Gao, Annunziato Amendola, Phinit Phisitkul, and John Femino. 2016. “Cortical Bone Thickness of the Distal Part of the Tibia Predicts Bone Mineral Density.” The Journal of Bone and Joint Surgery. American Volume 98 (9): 751–60. https://doi.org/10.2106/JBJS.15.00795.

Pobloth, Anne-Marie, Sara Checa, Hajar Razi, Ansgar Petersen, James C. Weaver, Katharina Schmidt-Bleek, Markus Windolf, et al., 2018. “Mechanobiologically Optimized 3D Titanium-Mesh Scaffolds Enhance Bone Regeneration in Critical Segmental Defects in Sheep.” *Science Translational Medicine* 10 (423): eaam8828. https://doi.org/10.1126/scitranslmed.aam8828.

Popov, Vladimir V., Gary Muller-Kamskii, Aleksey Kovalevsky, Georgy Dzhenzhera, Evgeny Strokin, Anastasia Kolomiets, and Jean Ramon. 2018. “Design and 3D-Printing of Titanium Bone Implants: Brief Review of Approach and Clinical Cases.” *Biomedical Engineering Letters* 8 (4): 337–44. https://doi.org/10.1007/s13534-018-0080-5.

Samiezadeh, Saeid, Pouria Tavakkoli Avval, Zouheir Fawaz, and Habiba Bougherara. 2014. “Biomechanical Assessment of Composite versus Metallic Intramedullary Nailing System in Femoral Shaft Fractures: A Finite Element Study.” *Clinical Biomechanics* 29 (7): 803–10. https://doi.org/10.1016/j.clinbiomech.2014.05.010.

Sanyal, Arnav, Atul Gupta, Harun H. Bayraktar, Ronald Y. Kwon, and Tony M. Keaveny. 2012. “Shear Strength Behavior of Human Trabecular Bone.” *Journal of Biomechanics* 45 (15): 2513–19. https://doi.org/10.1016/j.jbiomech.2012.07.023.

Verhulp, E., B. Van Rietbergen, R. Müller, and R. Huiskes. 2008. “Micro-Finite Element Simulation of Trabecular-Bone Post-Yield Behaviour – Effects of Material Model, Element Size and Type.” *Computer Methods in Biomechanics and Biomedical Engineering* 11 (4): 389–95. https://doi.org/10.1080/10255840701848756.

Weinkamer, Richard, Markus A. Hartmann, Yves Brechet, and Peter Fratzl. 2004. "Stochastic Lattice Model for Bone Remodeling and Aging." *Physical Review Letters* 93 (22): 228102. https://doi.org/10.1103/PhysRevLett.93.228102.

Wittig, James & Bickels, Jacob & Priebat, Dennis & Jelinek, James & Kellar-Graney, Kristen & Shmookler, Barr & Malawer, Martin. (2002). Osteosarcoma: A Multidisciplinary Approach to Diagnosis and Treatment. American family physician. 65. 1123-32.

Yang, Yi & Yang, Rui & Roth, Michael & Piperdi, Sajida & Zhang, Wendong & Dorfman, Howard & Rao, Pulivarthi & Park, Amy & Tripathi, Sandeep & Freeman, Carrie & Zhang, Yunjia & Sowers, Rebecca & Rosenblum, Jeremy & Geller, David & Hoang, Bang & Gill, Jonathan & Gorlick, Richard. (2017). Genetically transforming human osteoblasts to sarcoma: Development of an osteosarcoma model. Genes & Cancer. 8. 484-494. 10.18632/genesandcancer.133.

Zhang, Wenjie, Chun Feng, Guangzheng Yang, Guanglong Li, Xun Ding, Shaoyi Wang, Yuandong Dou, et al., 2017. "3D-Printed Scaffolds with Synergistic Effect of Hollow-Pipe Structure and Bioactive Ions for Vascularized Bone Regeneration." *Biomaterials* 135 (August): 85–95. https://doi.org/10.1016/j.biomaterials.2017.05.005.

Zhang, Ying, Leilei Zhang, Ruibo Sun, Yudong Jia, Xiantao Chen, Youwen Liu, Hong Oyang, and Lizhi Feng. 2018. "A New 3D Printed Titanium Metal Trabecular Bone Reconstruction System for Early Osteonecrosis of the Femoral Head." *Medicine* 97 (26). https://doi.org/10.1097/MD.0000000000011088.

Appendix A: Step Parameters for ABAQUS Simulations

Note that the following algorithmically appended to the end of the generated input file, using notation found in the ABAQUS User's Manual.

```
*Material, name=PLA
*Elastic
2.79e3, 0.35
*Density
1250
*Step, name = Step-1, nlgeom=No
*Static
1., 1., 1e-05, 1.
** BOUNDARY CONDITIONS
**
** Name: BC-1 Type: Symmetry/Antisymmetry/Encastre
*Boundary
fixed_nodes, ENCASTRE
*Boundary
moved_nodes, 3, 3, -1
*End Step
```

Appendix B: Custom Code

Appendix B-1: GenerateAbaqusModelFromSTL.java

Note that this file is dependent on base code written by the Coded Structures Laboratory at NASA Ames Research Center. The following custom codes were written under the guidance of Joseph Kim, a researcher at the Coded Structures Laboratory.

```
package com.libgdx.voxelbulletsim.Main.boneSim;

import com.libgdx.voxelbulletsim.General.NodeBeamCounter;
import com.libgdx.voxelbulletsim.General.STLConverter;
import com.libgdx.voxelbulletsim.Geometry.ABAFileWriter;
import com.libgdx.voxelbulletsim.Geometry.ABANode;
import com.libgdx.voxelbulletsim.Geometry.ABAVoxel;
import com.libgdx.voxelbulletsim.Geometry.Point;
import java.io.File;
import java.io.PrintWriter;
import java.util.ArrayList;

public class GenerateAbaqusModelFromSTL {
   private String material = "PLA";
   private int subdivisions = 1;
   private String dV = "1";
   public ABANode[] refNode;

   private String connectionMaterial = "Carbon";
   private double connectionBeamWidth = 0.1;

   private String inputDirectory = System.getProperty("user.dir") + File.separator + "stlInputs" +
File.separator;
   private String outputDirectory = System.getProperty("user.dir") + File.separator + "stlOutputs" +
File.separator;

   String fileName = "TibiaSection180.stl";

   public void runMain(double size, double beamWidth) {
      String bW = String.valueOf((int) Math.round(beamWidth*100));
      String sW = String.valueOf((int) Math.round(size));
      int numNodes = 0;

      // Create and clean output directory
      PrintWriter out = null;
      try {
         // Create output directory if it does not exist
         File checkDir = new File(outputDirectory);
         if (!checkDir.exists()) {
            checkDir.mkdir();   }
         // Generate output file
         out = new PrintWriter(outputDirectory + "P_" + sW + "_B_" + bW + "_D_" + dV + ".inp");
      } catch (Exception e) {
```

```
            e.printStackTrace();
            return;
        }

        STLConverter myConverter = new STLConverter(inputDirectory + fileName, (float)size, false, true,
false);

        System.out.println("STL converted to voxel points");
        Point[] voxelPoints = myConverter.getVoxelPoints();

        System.out.println("Total of " + voxelPoints.length + " voxel points");
        ArrayList<ABAVoxel> voxelList = new ArrayList<>();

        // Set node thickness for new voxel type
        ABAVoxel.setNodeMaterialSize("CarbonPlastic_thick", size, beamWidth);

        NodeBeamCounter myCounter = new NodeBeamCounter();
        int voxelID = 1;

        for (Point point: voxelPoints) {
            ABAVoxel newVoxel = new ABAVoxel(point, myCounter, voxelID++, size, beamWidth,
subdivisions, material, out);
            voxelList.add(newVoxel);
        }

        ABAVoxel.connect(voxelList);

        for (ABAVoxel voxel : voxelList) {
            for (ABANode node : voxel.mainNodes) {
                if (node.z < 3  ) {
                    node.nsets.add("moved_nodes");
                }
                if (node.z > 365) {
                    node.nsets.add("fixed_nodes");
                }
                numNodes += 1;
            }
        }
        System.out.println("Total of " + numNodes + " nodes");
        System.out.println("Voxel Size: " + size);

        ABAFileWriter myFile = new ABAFileWriter(voxelList, out);
        myFile.importMaterialFromFile(inputDirectory + "materialsHeavy.txt");
        myFile.importStepFromFile(inputDirectory + "step.txt");
        myFile.importLoadsFromFile(inputDirectory + "empty.txt");
        myFile.importBCFromFile(inputDirectory + "boneBcs.txt");
        myFile.importOutputsFromFile(inputDirectory + "outputs.txt");
        myFile.writeDefaultFileCustomElset();
        out.close();
    }
}
```

Appendix B-2: bulkStlInputs.java

This custom code loops through the code in Appendix C-1 to generate input files for any combination of desired parameters.

```
package com.libgdx.voxelbulletsim.Main.boneSim;

public class BulkStlInputs {
   public static void main(String[] args) {
      BulkStlInputs main = new BulkStlInputs();
      main.runMain();
   }

   public void runMain() {
      GenerateAbaqusModelFromSTL abaTest = new GenerateAbaqusModelFromSTL();
      for (int  i = 3; i < 10; i++) {
         abaTest.runMain(i,0.1);
         for (double j = 0.25; j <= 2; j = j + 0.25) {
            abaTest.runMain(i, j);
         }
      }
      for (int  i = 10; i <= 25; i = i + 3) {
         abaTest.runMain(i,0.1);
         for (double j = 0.25; j <= 2; j = j + 0.25) {
            abaTest.runMain(i, j);
         }
      }
   }
}
```

Appendix B-3: abaqusCommand.java

This custom code loops through the files generated by the code in Appendix C-2 to generate a single batch file for one click automatic simulation of all desired combinations.

```
package com.libgdx.voxelbulletsim.Main.boneSim;

import java.io.File;
import java.io.FileNotFoundException;
import java.io.PrintWriter;
import java.util.ArrayList;
import java.util.Iterator;

public class abaqusCommand {
   private String rootDirectory;
   public ArrayList<String> fileNames;

   public abaqusCommand() {
      this.rootDirectory = System.getProperty("user.dir") + File.separator + "stlOutputs" + File.separator;
      this.fileNames = new ArrayList();
   }

   public static void main(String[] args) {
      abaqusCommand main = new abaqusCommand();
      main.runMain();
   }

   public void getFiles(File[] files) {
      File[] var2 = files;
      int var3 = files.length;

      for(int var4 = 0; var4 < var3; ++var4) {
         File file = var2[var4];
         if (file.isDirectory()) {
            this.getFiles(file.listFiles());
         } else if (file.getName().contains(".inp") && file.getName().contains("D_1")) {
            this.fileNames.add(file.getName());
         }
      }
   }

   public void runMain() {
      PrintWriter out = null;

      try {
         out = new PrintWriter(this.rootDirectory + "runAbaqus.bat");
      } catch (FileNotFoundException var7) {
         var7.printStackTrace();}

      File[] files = (new File(this.rootDirectory)).listFiles();
      this.getFiles(files);
      int i = 0;
      Iterator var4 = this.fileNames.iterator();

      while(var4.hasNext()) {
```

```
            String fileName = (String)var4.next();
            ++i;
            String[] tokens = fileName.split("[.]");
            out.print("call abaqus job=");
            out.print(tokens[0]);
            if (i < this.fileNames.size()) {
               out.print(" interactive cpus=4\n");
            } else {
               out.print(" interactive cpus=4");
            }
         }

         out.close();
      }

   }
```

Appendix B-4: ProcessModulus.java

This custom code loops through the output databases generated by running the simulations via the code in Appendix C-3 to extract all desired information into a single spreadsheet using the code in Appendix C-5.

```
package com.libgdx.voxelbulletsim.Main.boneSim;

import java.io.*;
import java.util.ArrayList;
import java.util.Iterator;

public class ProcessModulus {
   private String rootDirectory;
   public ArrayList<String> fileNames;
   private PrintWriter out;

   public ProcessModulus() {
      this.rootDirectory = System.getProperty("user.dir") + File.separator + "stlOutputs" + File.separator;
      this.fileNames = new ArrayList();
   }

   public static void main(String[] args) {
      ProcessModulus main = new ProcessModulus();
      main.runMain();
   }

   public void getFiles(File[] files) {
      File[] var2 = files;
      int var3 = files.length;

      for(int var4 = 0; var4 < var3; ++var4) {
         File file = var2[var4];
         if (file.isDirectory()) {
            this.getFiles(file.listFiles());
         } else if (file.getName().contains(".dat")) {
            this.fileNames.add(file.getPath());
         }
      }
   }

   public void runMain() {
      PrintWriter out = null;
      try {
         // Create output directory if it does not exist
         File checkDir = new File(rootDirectory);
         if (!checkDir.exists()) {
            checkDir.mkdir();
         }
      } catch (Exception e) {
         e.printStackTrace();
         return;
      }
      File[] files = (new File(this.rootDirectory)).listFiles();
      this.getFiles(files);
```

```
        try {
            this.out = new PrintWriter(this.rootDirectory + "processedResults.csv");
        } catch (FileNotFoundException var35) {
            var35.printStackTrace();
        }

        CSVOutput csvOutput = new CSVOutput();
        Iterator var10 = this.fileNames.iterator();

        while(var10.hasNext()) {
            String fileName = (String)var10.next();
            String[] fileTokens = fileName.split("[\\\\|/]");
            String[] tokens = fileTokens[fileTokens.length - 1].split("[_.]");
            Double voxelSize = Double.parseDouble(tokens[1]);
            Double beamWidth = Double.parseDouble(tokens[3]);
            Double displacement = Double.parseDouble(tokens[5]);

            try {
                BufferedReader br = new BufferedReader(new FileReader(fileName));
                boolean started = false;
                boolean timeStarted = false;
                double stress = 0.0D;
                double modulus = 0D;

                for(String line = br.readLine(); line != null; line = br.readLine()) {
                    if (line.contains("ELEMENT  PT SEC FOOT-   MISES")) {
                        started = true;
                    }

                    if (started) {
                        String[] dataTokens;
                        if (line.contains("MAXIMUM")) {
                            dataTokens = line.trim().split(",");
                            dataTokens = dataTokens[0].split(" +");
                            stress = Double.parseDouble(dataTokens[1]);
                            modulus = stress*365;
                            modulus = Math.floor(modulus*100)/100;
                            timeStarted = true;
                        } else if (timeStarted && line.trim().startsWith("ELEMENT")) {
                            dataTokens = line.trim().split(" +");
                            Double maxElement = Double.parseDouble(dataTokens[1]);
                            csvOutput.addData(voxelSize + "," + beamWidth + "," + displacement + "," + stress + ","
+ maxElement + "," + modulus);
                            timeStarted = false;
                        }
                    }
                }
            } catch (Exception var36) {
                var36.printStackTrace();
            }
        }

        csvOutput.writeFile(this.out);
        this.out.close();
    }
```

Appendix B-5: CSVOutput.java

```
package com.libgdx.voxelbulletsim.Main.boneSim;

import java.io.PrintWriter;
import java.util.ArrayList;
import java.util.Iterator;

public class CSVOutput {
   private String header = "Voxel Size, Beam Width, Displacement (mm), Stress (MPa), Element Number,
Modulus (MPa)";
   private ArrayList<String> data = new ArrayList();

   public CSVOutput() {
   }

   public void addData(String dataLine) {
      this.data.add(dataLine);
   }

   public void writeFile(PrintWriter out) {
      out.println(this.header);
      Iterator var2 = this.data.iterator();

      while(var2.hasNext()) {
         String dataLine = (String)var2.next();
         out.println(dataLine);
      }

   }
}
```

Biography

Afsheen Sajjadi was born in Columbia, SC on October 14, 1996, to Nahid and Habib Sajjadi. He has an older sister Auzita. He earned his high school diploma at Ovey Comeaux High School in Lafayette, LA. Staying close by, Afsheen entered Tulane University in New Orleans, LA as an undergraduate student in 2015 to study Biomedical Engineering. Afsheen continued his studies at Tulane as a master's student. After graduation, Afsheen plans to pursue a Ph.D in Biomedical Engineering at Northwestern University to work on the cutting edge of rehabilitation robotics at the intersection of biomechanics and robotics.